

DRAFT

CMS Paper

The content of this note is intended for CMS internal use and distribution only

2020/06/09

Archive Hash: dbd7634-D

Archive Date: 2020/06/09

Measurement of differential $t\bar{t}$ production cross sections in the full kinematic range using lepton+jets events from pp collisions at $\sqrt{s} = 13$ TeV

The CMS Collaboration

Abstract

Measurements of differential and double-differential cross sections of the production of top quark pairs ($t\bar{t}$) are presented in the lepton+jets channels with a single electron or muon and jets in the final state. The analysis combines signatures of top quarks with low transverse momentum p_T , where the top decay products can be identified as separated jets and isolated leptons, and with high p_T , where the decay products are collimated and overlap. With this combination implicit selections of the top quark p_T are avoided and the full p_T range is probed. The measurements are based on data collected by the CMS experiment at the LHC between 2016 and 2018 corresponding to an integrated luminosity of 137 fb^{-1} . The cross sections are presented at parton and particle level, where the later minimizes extrapolations based on theoretical assumptions. Both results are compared to various kinds of standard model calculation using different combinations of matrix elements and parton shower models. In general, decent agreements between the measurements and the predictions are observed. The next-to-next-to-leading order quantum chromodynamics (QCD) calculation with its reduced uncertainty provides an improved description of the measurements compared to next-to-leading order QCD calculations. From the integration of the differential cross sections an inclusive $t\bar{t}$ production cross section of $\sigma_{\text{tot}} = 815 \pm 25 \text{ pb}$ is obtained.

This box is only visible in draft mode. Please make sure the values below make sense.

PDFAuthor: Otto Heinz Hindrichs
PDFTitle: Differential $t\bar{t}$ cross sections in the full kinematic range in lepton+jets
PDFSubject: CMS
PDFKeywords: CMS, physics, your topics

Please also verify that the abstract does not use any user defined symbols

1 Introduction

We present measurements of differential top quark pair ($t\bar{t}$) production cross sections in the e/μ +jets channels, i.e., with a single electron or muon and jets in the final state. Precision measurements of $t\bar{t}$ production are important tests of the standard model (SM), since the top quark with its high mass and its property of being the only quark that can be observed before hadronization, plays an exceptional role. With its strong coupling to the Higgs boson it might be involved in beyond SM scenarios of electroweak symmetry breaking. These could become visible in altered kinematic distributions of $t\bar{t}$ production. A detailed understanding of $t\bar{t}$ production is also important for many searches for beyond SM phenomena, where it often forms an important background. In addition, it is shown in (TOP-18-004)TODO that differential $t\bar{t}$ production can contribute significantly to the measurement of parton distribution functions (PDF).

At the CERN LHC measurements of differential cross sections have been performed in various $t\bar{t}$ decay channels at pp collision energies of 7 TeV [1, 2], 8 TeV [3–9], and 13 TeV [10–17].

This analysis is based on 137 fb^{-1} recorded in LHC Run 2, where 35.9 fb^{-1} were recorded in 2016, 41.5 fb^{-1} in 2017, and 59.7 fb^{-1} in 2018. Since the running conditions and the CMS detector changed with the years, performance and calibration measurements are performed separately for each year.

We use techniques of resolved $t\bar{t}$ reconstruction introduced in previous CMS analyses [13, 14]. These are applicable if all $t\bar{t}$ decay products can be reconstructed as separated leptons and jet in the detector typically for top quarks with $p_T < 500\text{ GeV}$. These results are extended adding the information of boosted top quarks, whose decay products are collimated and overlap. Reconstruction techniques for both, the hadronically (t_h) and the leptonically (t_ℓ) decaying boosted top quarks, are developed and combined with the resolved reconstruction. Finally, the differential cross sections are extracted performing a combined likelihood fit to several categories of different reconstruction methods and lepton flavors in the three years of data taking. The combinations of the different categories allow for constraints of systematic uncertainties and result in an improved precision with respect to previous measurements.

The differential cross sections are presented at parton and particle levels. The parton level is represented by a $t\bar{t}$ pair before it decays. In other words, the top quarks are assumed to be stable and all effects related to their decays have to be taken into account by the measurement. The cross sections are presented in the full phase space of the top quarks. This means for the parton-level measurements all effects related to top quark decays, hadronization, and limited detector acceptance of the decay products are corrected based on theoretical assumptions. These extrapolations can be reduced in the particle-level measurements, where the $t\bar{t}$ pair is defined based on jets and leptons that can be observed in the detector. All details about the particle-level top quarks are given in Section 3.

At the parton level we measure the differential cross sections as a function of the following variables: $p_T(t_h)$, $p_T(t_\ell)$, their scalar sum S_T , the transverse momentum of leading $p_T(t_{\text{high}})$ and trailing $p_T(t_{\text{low}})$ of top quarks, $|y(t_h)|$, $|y(t_\ell)|$, rapidity differences $\Delta|y_{t/\bar{t}}| = |y(t) - |y(\bar{t})|$, $|\Delta y_{t/\bar{t}}| = |y(t) - y(\bar{t})|$, the angle between the top quarks in the transverse plane $\Delta\phi_{t/\bar{t}}$; $|y(t\bar{t})|$, the mass $M(t\bar{t})$, and $p_T(t\bar{t})$; $\cos(\theta^*)$, where θ^* is the angle between the t and the direction of flight of the $t\bar{t}$ system calculated in the $t\bar{t}$ rest-frame. Double differential cross sections are measured as functions of several combinations of these variables: $p_T(t_h)$ vs. $|y(t_h)|$, $M(t\bar{t})$ vs. $|y(t\bar{t})|$, $M(t\bar{t})$ vs. $\cos(\theta^*)$, $M(t\bar{t})$ vs. $p_T(t_h)$, $M(t\bar{t})$ vs. $\Delta|y_{t/\bar{t}}|$, $|\Delta y_{t/\bar{t}}|$ vs. $M(t\bar{t})$, and $|y(t)|$ vs. $|y(\bar{t})|$. From the integration of the differential cross sections a precise measurement of the inclusive $t\bar{t}$ pro-

duction cross section is obtained. In addition, at particle level the cross sections of jet multiplicities and differential cross section as function of $p_T(t_h)$, $M(t\bar{t})$, and $p_T(t\bar{t})$ in bins of jet multiplicity are determined. Finally, the differential cross section as function of the scalar sum of the p_T of additional jets H_T , the invariant mass of the top quarks and all additional jets M_{evt} , and the p_T of the electron and muons $p_T(\ell)$ are presented.

We begin with an overview of the used theoretical calculations and simulations of the detector in Section 2, followed by the detailed discussion of the particle-level definitions in Section 3. After a short description of the CMS detector and the reconstruction and identification of the involved physics objects in Section 4 and 5, respectively, the resolved and boosted reconstructions of t_h and t_ℓ are detailed in Sections 6–8. An overview of the event categorization is presented in Section 9 before the methods of background subtraction are explained in Section 10 for the categories of resolved reconstruction and in Section 11 for the boosted reconstructions. Afterwards the cross sections are finally extracted in Section 12. In Section 13 detailed information about systematic uncertainties can be found. The results at parton and particle levels are presented and discussed in Sections 14. The paper is summarized in Section 15.

2 Signal and background modeling

The Monte Carlo generator POWHEG [18–21] (h_vq) is used to simulate the production of $t\bar{t}$ events at NLO accuracy in quantum chromodynamics (QCD). The POWHEG output is combined with the parton shower (PS) simulation of PYTHIA8 [22, 23] using the underlying event tune CUETP8M2T4 [24, 25] for the 2016 simulations and the CP5 tune for the 2017 and 2018 simulations. The renormalization μ_r and factorization μ_f scales are set to the transverse mass $m_T = \sqrt{m_t^2 + p_T^2}$ of the top quark, where a top quark mass $m_t = 172.5 \text{ GeV}$ is used. The parametrizations of PDFs are NNPDF30_nlo_as.0118 [26] and NNPDF31_nnlo_as.0118 [27] for 2016 and 2017/2018, respectively.

The detector response is simulated using GEANT4 [28]. The simulations include multiple pp interactions per bunch crossing (pileup). The simulated distribution of pileup events corresponds to the distribution in data for each year. Finally, the same reconstruction algorithms that are applied to the data are used for the simulated events. This simulation is the default to obtain all corrections for the extraction of the cross sections.

For uncertainty estimations a couple of variations to the default simulation are used. This includes simulations with m_t varied by 1 GeV, the parton shower matching scale h_{damp} varied around the central values of $1.58^{+0.66}_{-0.59} m_t$ (CUETP8M2T4) and $1.38^{+0.92}_{-0.51} m_t$ (CP5) by the uncertainties obtained from the PS tune, and variations of the hadronization model parameters. In addition, a simulation with a different color reconnection model that allows the color reconnection from resonances, is used. Distributions that correspond to variations of the scales μ_r , μ_f , or the PS scales by factors of two are obtained by applying different event weights to the default simulation. Different event weights are also used for the estimation of PDF uncertainties.

The measured differential cross sections are compared to the prediction obtained by POWHEG+HERWIG [29] (v2.7.1) with tune CH5 (GEN-19-001)TODO. In addition, MADGRAPH5_aMC@NLO [30] (v2.2.2) (MG5_aMC@NLO) is used to simulate $t\bar{t}$ events with additional partons. All processes with up to two additional partons are calculated at NLO QCD and combined with the PYTHIA8 PS simulation using the FxFx [31] algorithm.

All $t\bar{t}$ simulations are normalized to an inclusive $t\bar{t}$ production cross section of $832^{+40}_{-46} \text{ pb}$ calculated with top++2.0 [32]. This value is calculated with next-to-NLO (NNLO) accuracy, includ-

ing the resummation of next-to-next-to-leading-logarithmic soft-gluon terms. Its uncertainty is evaluated by varying the choice of μ_r and μ_f and by propagating uncertainties in the PDFs. Differential cross sections with NNLO QCD accuracy are obtained with MATRIX [33], where $\mu_r = \mu_f = \frac{1}{2}(\sqrt{m_t^2 + p_T^2(t)} + \sqrt{m_t^2 + p_T^2(\bar{t})})$ and the PDF NNPDF31_nnlo.as_0118 is used.

The main backgrounds are simulated using the same techniques. The MG5_aMC@NLO generator is used for the simulation of W boson production in association with jets, t -channel single top quark production, and Drell–Yan (DY) production in association with jets. The generator POWHEG [34] is used for the simulation of single top quark associated production with a W boson (tW), and PYTHIA8 is used for multijet production. In all cases, the PS and the hadronization are described by PYTHIA8. The W boson and DY backgrounds are normalized to their NNLO cross sections calculated with FEWZ [35] (v3.1). The t -channel single top quark production is normalized to the NLO calculation obtained from HATHOR [36] (v2.1). The production of tW is normalized to the NLO calculation [37], and the multijet simulation is normalized to the LO calculation obtained with PYTHIA8 [23].

3 Definitions at particle level

The definitions of particle-level objects constructed from simulated particles with a mean lifetime greater than 30 ps, obtained from the predictions of $t\bar{t}$ event generators before any detector simulation, are summarized below. These particle-level objects are further used to define the particle-level top quarks. Detailed studies on particle-level definitions can be found in Ref. [38].

- All simulated electrons and muons, that do not originate from the decay of a hardron in the final state, are corrected for effects of bremsstrahlung by adding the photon momenta to the momentum of the closest lepton if their separation is $\Delta R < 0.1$, where $\Delta R = \sqrt{\Delta^2\eta + \Delta^2\phi}$. All photons are considered for the momentum correction. In addition, we require the corrected lepton to have $p_T > 15 \text{ GeV}$ and $|\eta| < 2.4$.
- All neutrinos are selected including those stemming from decays of hadrons.
- Jets are clustered by the anti- k_T jet algorithm [39, 40] with a distance parameter of 0.4. All particles with the exception of neutrinos are clustered. Jets with $p_T > 25 \text{ GeV}$ and $|\eta| < 2.4$ are selected if there is no electron or muon, as defined above, within $\Delta R = 0.4$.
- b jets at the particle level are defined as those jets that contain a b hadron. As a result of the short lifetime of b hadrons only their decay products are considered for the jet clustering. However, to allow their association with a jet, the b hadrons are also included with their momenta scaled down to a negligible value. This preserves the information of their directions, but removes their impact on the jet clustering.
- Candidates of a boosted t_ℓ are b jets that would be rejected by the lepton cleaning, i.e., there is a selected lepton within the jet cone of $\Delta R < 0.4$. A $p_T > 50 \text{ GeV}$ is required for the lepton. The candidate momentum is calculated as the sum of the momenta of the jet, the lepton, and all selected neutrinos. It is ensured that the lepton momentum is not counted twice if it is a constituent of the jet. Finally, a $p_T > 400 \text{ GeV}$ and $|\eta| < 2.4$ is required for the candidate.
- Candidates of a boosted t_h are jets defined exactly as the b jets above but clustered and cleaned from leptons with a distance parameter of 0.8. In addition, the invariant mass of all constituents M_{jet} is required to be greater than 120 GeV with $p_T > 400 \text{ GeV}$ and $|\eta| < 1.6$.

Based on the invariant masses of these objects, we construct a pair of particle-level top quarks in the e/μ +jets final state. Events with exactly one electron or muon with $p_T > 30$ GeV and $|\eta| < 2.4$ are selected. Simulated events with an additional selected electron or muon are rejected.

If one candidate for a boosted t_ℓ and at least one candidate for a boosted t_h exist, the boosted t_h with M_{jet} closest to m_t is selected and the two form the pair of particle-level top quarks. If there is a boosted t_ℓ but no candidate of a boosted t_h , the event is rejected. A combination of a boosted t_ℓ and a resolved reconstruction of a t_h is, in analogy to the detector-level reconstruction, not considered.

If there is no boosted t_ℓ , we take the sum of the four-momenta of all neutrinos as the neutrino candidate momentum p_ν from t_ℓ decay and find the permutation of jets that minimizes the quantity

$$[M(p_\nu + p_\ell + p_{b_\ell}) - m_t]^2 + [M(p_{j_{W1}} + p_{j_{W2}}) - m_W]^2 + [M(p_{j_{W1}} + p_{j_{W2}} + p_{b_h}) - m_t]^2, \quad (1)$$

where $p_{j_{W1,2}}$ are the four-momenta of two light-flavor jet candidates, considered as the decay products of the hadronically decaying W boson; $p_{b_{\ell,h}}$ are the four-momenta of two b jet candidates; p_ℓ is the four-momentum of the lepton; and $m_W = 80.4$ GeV [41] is the mass of the W boson. All jets with $p_T > 25$ GeV and $|\eta| < 2.4$ are considered. At least four jets are required, of which at least two must be b jets. The remaining jets with $p_T > 30$ GeV and $|\eta| < 2.4$ are defined as additional jets.

Alternatively, we also evaluate the possibility of a selection with boosted t_h by minimizing

$$[M(p_\nu + p_\ell + p_{b_\ell}) - m_t]^2 + [M_{\text{jet}} - m_t]^2, \quad (2)$$

If both reconstruction methods, for the resolved and the boosted t_h , are successful, we select the reconstruction for which $M(t_h)$ is closer to m_t .

Events with a hadronically and a leptonically decaying particle-level top quark are not required to be e/μ +jets events at the parton level, e.g., $t\bar{t}$ dilepton events with additional jets can be identified as e/μ +jets event at the particle level if one lepton fails to pass the selection. As an example, the comparison between the $p_T(t_h)$ distributions at the particle and parton levels are shown in Fig. 1 and demonstrates the direct relation between particle-level and parton-level top quarks. Overall a good correspondence between the particle level and the parton level is observed. This ensures that the observables are sensitive to the underlying physics of $t\bar{t}$ production.

4 The CMS detector

The central feature of the CMS detector is a superconducting solenoid of 6 m internal diameter, providing a magnetic field of 3.8 T. Within the solenoid volume are a silicon pixel and strip tracker, a lead tungstate crystal electromagnetic calorimeter (ECAL), and a brass and scintillator hadron calorimeter (HCAL), each composed of a barrel and two endcap sections. Forward calorimeters extend the η coverage provided by the barrel and endcap detectors. Muons are measured in gas-ionization detectors embedded in the steel flux-return yoke outside the solenoid. A more detailed description of the CMS detector, together with a definition of the coordinate system and relevant kinematic variables, can be found in Ref. [42].

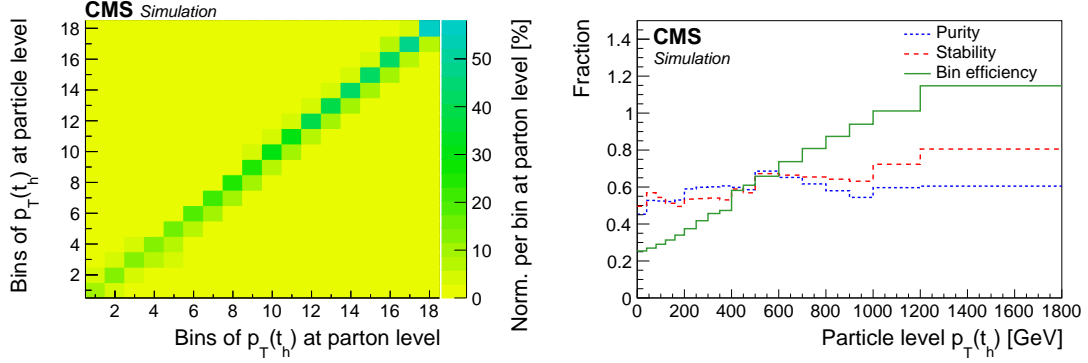


Figure 1: Comparison between the $p_T(tqh)$ distributions at the particle and parton level, extracted from the POWHEG+PYTHIA8 simulation. Left: p_T -bin migrations between particle and parton level. The p_T range of the bins can be taken from the right panel. Each column is normalized such that the sum of its entries corresponds to the fraction of particle-level events in this bin at the parton level in the full phase space. Right: fraction of parton-level top quarks in the same p_T bin at the particle level (purity), fraction of particle-level top quarks in the same p_T bin at the parton level (stability), ratio of the number of particle- to parton-level top quarks (bin efficiency).

The particle-flow (PF) event algorithm [43] reconstructs and identifies each individual particle with an optimized combination of information from the various elements of the CMS detector. The energy of muons is obtained from the curvature of the corresponding track. The energy of electrons is determined from a combination of the electron momentum at the primary interaction vertex as determined by the tracker, the energy of the corresponding ECAL cluster, and the energy sum of all bremsstrahlung photons spatially compatible with originating from the electron track. The energy of photons is directly obtained from the ECAL measurement, corrected for zero-suppression effects. The energy of charged hadrons is determined from a combination of their momentum measured in the tracker and the matching ECAL and HCAL energy deposits, corrected for zero-suppression effects and for the response function of the calorimeters to hadronic showers. Finally, the energy of neutral hadrons is obtained from the corresponding corrected ECAL and HCAL energy.

5 Physics object reconstruction

The measurements presented in this paper depend on the reconstruction and identification of muons, electrons, jets, and missing transverse momentum associated with a neutrino. Muons and electrons are selected if they are compatible with originating from the primary vertex, which, among the reconstructed primary vertices, is the one with the largest value of summed physics-object p_T^2 . The physics objects are jets, clustered using the jet finding algorithm [39, 40] with the tracks assigned to the primary vertex as inputs, and the associated missing transverse momentum, taken as the negative vector sum of the \vec{p}_T of those jets.

Isolated electrons and muons with $p_T > 30$ GeV and $|\eta| < 2.4$ are selected. Only in 2018 the minimum p_T of electrons is raised to 34 GeV due to increased thresholds of the trigger. Several quality criteria including isolation and compatibility with the selected primary vertex are required. The muon and electron reconstruction and selection efficiencies are measured in the data using tag-and-probe techniques [44–46]. Depending on the p_T and η , their product is 75–85% for muons and 50–80% for electrons. The nonisolated electrons and muons are required to have $p_T > 50$ GeV. For lower p_T the rate of nonisolated leptons from backgrounds is very high

and cannot be handled by the trigger. Apart from the p_T and isolation requirements the non-isolated electrons and muons have to fulfill the same selection criteria as the isolated leptons. Their reconstruction and trigger efficiencies are also measured in $t\bar{t}$ dilepton events.

Jets are clustered from PF objects using the anti- k_T jet algorithm with a distance parameter of 0.4 implemented in the FASTJET package [40]. Charged particles originating from a pileup interaction vertex are excluded. The total energy of the jets is corrected for energy depositions from pileup. In addition, p_T - and η -dependent corrections are applied to correct for the detector response effects [47]. If an isolated lepton with $p_T > 15$ GeV within $\Delta R = 0.4$ around a jet exists, the jet is assumed to represent the isolated lepton and is removed from further consideration. Jets are considered for analysis if they fulfill the kinematic requirements of $p_T > 30$ GeV and $|\eta| < 2.4$.

For the identification of b jets, the DeepCSV algorithm [48] is used. It provides a discriminant between b and other-flavored jets based on the information of secondary vertices and the impact parameter of tracks at the primary vertex combined with an artificial neural network (NN). A jet is identified as a b jet if the associated value of the discriminant exceeds a threshold criterion. Two different selection criteria are used: a tight with an efficiency of about 70–75% and a rejection probability of about 99% for other-flavored jets, and a loose with corresponding values of 85–90% and 90%.

Boosted t_h candidates are identified as anti- k_T jets with a size parameter of 0.8, $p_T > 400$ GeV, $|\eta| < 1.6$, and a jet mass $M_{\text{jet}} > 120$ GeV. The jets are based on the PUPPI [49] algorithm for pileup subtraction and the p_T of all PF constituents are rescaled according to their PUPPI weights before clustering.

The missing transverse momentum \vec{p}_T^{miss} is calculated as the negative of the vectorial sum of transverse momenta of all PF candidates in the event. Jet energy corrections are also propagated to improve the measurement of \vec{p}_T^{miss} .

6 Resolved reconstruction of the top quark-antiquark system

For the resolved reconstruction exactly one isolated electron or muon and at least four jets are required. If at least two of the jets are identified as b jets by the tight criterion, the event is categorized as “2t”. If there is one jet passing the tight and another jet passing the loose b-tagging criteria, the event falls into the “1t1l” category.

The reconstruction of the $t\bar{t}$ system in the resolved case follows closely the methods used in previous CMS analyses [13, 14]. The goal is the correct identification of detector-level objects as top quark decay products. All possible permutations of assigning detector-level jets to the corresponding $t\bar{t}$ decay products are tested and a likelihood that a certain permutation is correct is evaluated. Only the two jets with the highest b identification probabilities are tested as b_ℓ and b_h candidates. In each event, the permutation with the highest likelihood is selected.

For all tested permutation the neutrino four-momentum p_ν is reconstructed using the “Neutrino-Solver” algorithm [50]. The idea of this algorithm is to find all possible solutions for the three components of the neutrino momentum vector using the two mass constraints $(p_\nu + p_\ell)^2 = m_W^2$ and $(p_\nu + p_\ell + p_{b_\ell})^2 = m_t^2$. Each equation describes an ellipsoid in the three-dimensional momentum space of the neutrino. The intersection of these two ellipsoids is usually an ellipse. We select p_ν as the point on the ellipse for which the distance $D_{\nu,\text{min}}$ between the ellipse projection onto the transverse plane and \vec{p}_T^{miss} is minimal. This algorithm leads to a unique solution for the longitudinal neutrino momentum and an improved resolution of its transverse component.

For the cases where the invariant mass of the lepton and b_ℓ candidate is above m_t no solution can be found and the corresponding permutation is discarded. The minimum distance $D_{\nu,\min}$ is also used to identify the correct b_ℓ , as described below.

The value of $D_{\nu,\min}$ from the neutrino reconstruction and the mass constraints on the hadronically decaying top quark are combined in a likelihood function λ , given by

$$-\log[\lambda] = -\log[P_m(m_2, m_3)] - \log[P_\nu(D_{\nu,\min})], \quad (3)$$

where P_m is the two-dimensional probability density of the invariant masses of the W bosons and the top quarks that are correctly reconstructed. The value of λ is maximized to select the permutation of jets. The probability density P_m is calculated as a function of the invariant mass of the two jets, m_2 , tested as the W boson decay products, and the invariant mass of the three jets, m_3 , tested as the decay products of the t_h . The distributions for the correct jet assignments, taken from the POWHEG+PYTHIA8 simulation and normalized to unit area, are shown in Fig. 2. This part of the likelihood function is sensitive to the correct reconstruction of the t_h . For the $2t(1t1l)$ category $-\log[P_m(m_2, m_3)] < 11(9)$ is required. This selection rejects about 50% of the multijet, W boson, and single top quark backgrounds. For higher values of $-\log[P_m(m_2, m_3)]$ almost all $t\bar{t}$ events are reconstructed incorrectly and are considered for a boosted reconstruction.

The probability density P_ν describes the distribution of $D_{\nu,\min}$ for a correctly selected b_ℓ . In Fig. 2 the normalized distributions of $D_{\nu,\min}$ for b_ℓ and for other jets are shown. On average, the distance $D_{\nu,\min}$ for a correctly selected b_ℓ is smaller and has a smaller tail compared to the distance obtained for other jets. Permutations with values of $D_{\nu,\min} > 150$ GeV are rejected since they are very unlikely to originate from a correct b_ℓ association. This part of the likelihood function is sensitive to the correct reconstruction of the t_ℓ .

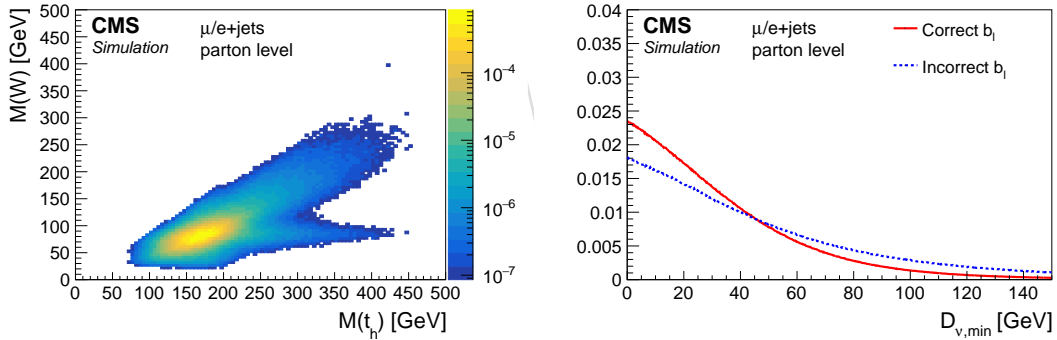


Figure 2: Normalized two-dimensional mass distribution of the correctly reconstructed hadronically decaying W bosons and the correctly reconstructed t_h (left). Normalized distributions of the distance $D_{\nu,\min}$ for correctly and incorrectly selected b jets from the t_ℓ (right). The distributions are taken from the POWHEG+PYTHIA8 $t\bar{t}$ simulation.

A comparison of data to the simulation of variables related to the reconstruction of the resolved $t\bar{t}$ system are shown in Figs. 3 and 4 for the $2t$ and $1t1l$ categories, respectively. Here the $t\bar{t}$ simulation is split into different categories based on the success of the reconstruction. The category “ $t\bar{t}$ correct” contains all events with all decay products correctly identified, “ $t\bar{t}$ wrong” are incorrectly reconstructed, but all decay products are available, and “ $t\bar{t}$ nonreconstructable” are events with at least one missing decay product caused by detector inefficiencies or acceptance losses. Finally, “ $t\bar{t}$ non signal” are $t\bar{t}$ background events, e.i., depending on the measurement no parton- or particle-level $t\bar{t}$ pair in the desired decay channel and phase space exists.

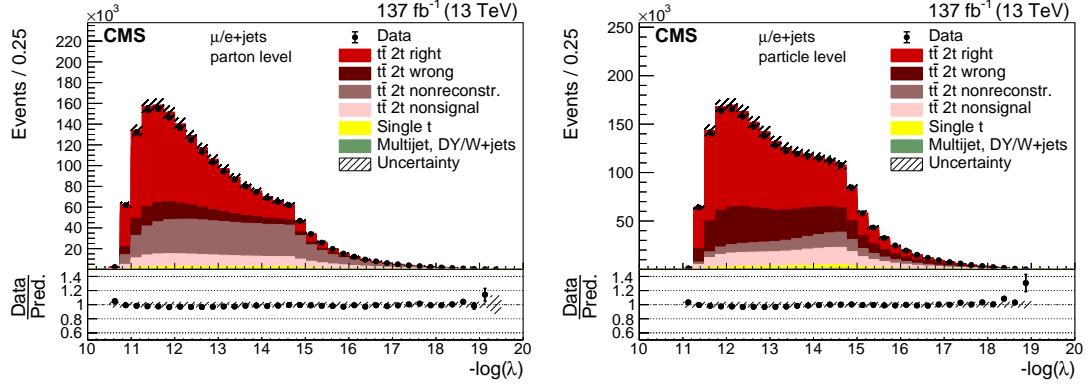


Figure 3: Comparison of data and simulation of variables related to the resolved reconstruction in the 2m category. The hatched uncertainty shows the statistical uncertainties in the prediction.

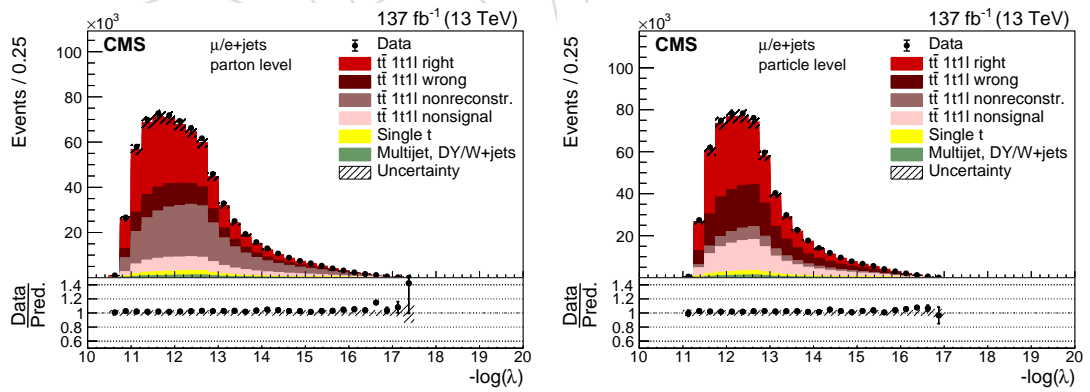


Figure 4: Comparison of data and simulation of variables related to the resolved reconstruction in the 1m1l category. The hatched uncertainty shows the statistical uncertainties in the prediction.

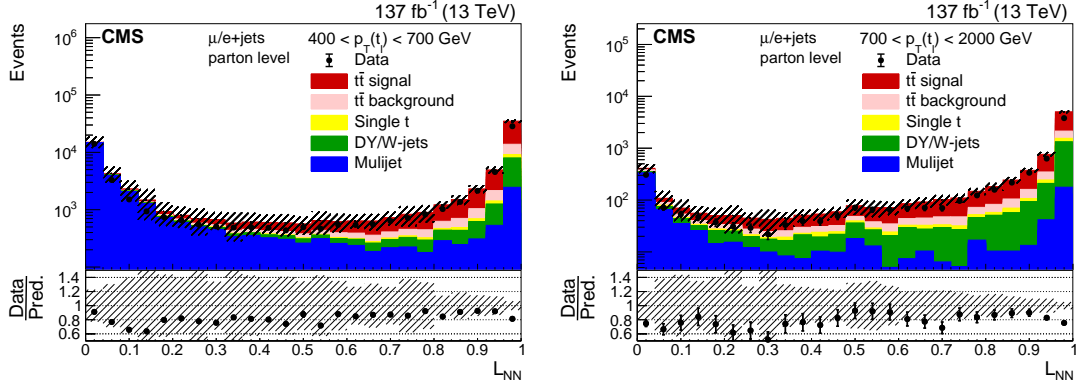


Figure 5: Distributions of the output variable of the NN for the identification of a boosted t_ℓ . The distributions are shown in low (left) and high (right) p_T -regions.

7 Identification and reconstruction of boosted leptonically decaying top quarks

For $p_T(t_\ell) > 400 \text{ GeV}$ the separation between the lepton and the b jet becomes increasingly small and the isolation cone of the lepton starts overlapping with constituents of the b jet. In this case the leptons do not fulfill the standard isolation criterion. Therefore, nonisolated leptons are used for the reconstruction of the boosted t_ℓ . We look for a loosely b -tagged jet within $\Delta R = 0.6$ around such a lepton. If the lepton is a constituent of the jet, its momentum is subtracted from the jet momentum to avoid a double counting. Afterwards, p_ℓ is determined using the Neutrino-Solver algorithm as introduced in Section 6. If the resulting p_T sum of the lepton, the b jet, and the neutrino is $> 400 \text{ GeV}$, we consider this as a boosted t_ℓ candidate. Candidates that are incompatible with the mass constraints imposed by the Neutrino-Solver are removed with the requirement of $D_\nu < 150 \text{ GeV}$. The transverse and longitudinal momentum resolution is about 10% for the whole p_T range.

The reconstructed candidates might be jets containing a lepton from a hadron decay or from a leptonically decaying W boson produced within the jet. Based on the following variables we use a NN to discriminate between top quark and background candidates: the invariant mass of the lepton and the b jet $M(\ell, b \text{ jet})$, $M_{b \text{ jet}}/M(\ell, b \text{ jet})$, $p_T(\ell)/p_T(\ell + b \text{ jet})$, I_{far}/I_0 , and I_{near}/I_0 with the isolation variables $I = \sum_{\text{PF objects}} p_T(\text{PF obj.}) \Delta R^q(\ell, \text{PF obj.})$ with $q = -2, 0, 2$ for I_{near} , I_0 , and I_{far} , respectively. The distribution of the output variable L_{NN} of the NN is shown in Fig. 5. It is efficient in reducing the multijet background, while W bosons produced within a jet are more difficult to distinguish from the boosted t_ℓ . We select t_ℓ candidates with $L_{\text{NN}} > 0.7$. This requirement corresponds to a signal efficiency of 87% at p_T around 500 GeV decreasing slightly toward higher p_T , with about 80% efficiency at $p_T = 1000 \text{ GeV}$.

8 Identification and reconstruction of boosted hadronically decaying top quarks

All selected PUPPI jets are considered as t_h candidates. To discriminate candidates containing top decay products from other jets, several properties are combined using a NN. Most of these quantities are calculated after boosting the jet constituents into their center-of-mass system and clustering them with the anti- k_T jet algorithm with a size parameter of 0.5 to obtain a couple of sub-jets. Since these sub-jets are clustered in the center-of-mass frame and not in the laboratory

frame, the special treatment of longitudinal and transverse components of the momentum is not meaningful. Therefore, instead of the longitudinal boost invariant variables p_T and ΔR , the energy and the angle between objects are used in the jet-definition. We use the following input variables:

- From all combinations of two sub-jets calculate the invariant mass and use as input variables the three highest.
- The number of combinations of two sub-jets whose invariant masses exceed 40 GeV (pairs).
- From all combinations of three sub-jets calculate the invariant mass and use the two highest.
- The ratio of the highest invariant mass of three sub-jets over the mass of all constituents.
- The ratios of n-jettiness τ_2/τ_1 , τ_3/τ_2 , τ_4/τ_3 , and τ_5/τ_4 with $\tau_N = c \sum_k \min(q_1 \cdot p_k, q_2 \cdot p_k, \dots, q_N \cdot p_k)$, where q_i with $1 \leq i \leq N$ are the momenta of the N leading jets and p_k are the momenta of all constituent in the rest-frame.
- The energy of the four highest energetic sub-jets.
- The triple-product of the three leading normalized sub-jet momenta.
- The sphericity of all sub-jets. The sphericity $s = \frac{3}{2}(\lambda_2 + \lambda_3)$ with λ_2 and λ_3 the second and third highest eigenvalues of the tensor $S^{\alpha\beta} = \frac{\sum_i p_i^\alpha p_i^\beta / |p_i|}{\sum_i |p_i|}$, where p_i are the momenta of the sub-jets in the rest-frame and α, β are the spatial indices.
- Reboost the three leading sub-jets in the laboratory frame and calculate their momentum fractions of the whole jet.

We always find at least three sub-jets (isolated leptons are removed from the jet collection). Some of the variables rely on at least four sub-jets. Those are set to zero in the very rare cases where a fourth sub-jet is missing.

We consider two types of top candidates, “3Q” and “2Q”, where three(two) of the quarks from the t_h decay are within $\Delta R = 0.8$ of a 3Q(2Q) candidate. The 2Q candidates represent a significant contribution at intermediate transverse momentum ($p_T < 600$ GeV). They are in general more difficult to distinguish from background, but their momentum response and resolution is not significantly worse than those of 3Q candidates. In Fig. 6 the performance of the NN is demonstrated showing the background vs. signal selection efficiency. Distributions of the output of the NN H_{NN} can be found in Fig. 9, where the H_{NN} is used in template fits for background subtraction.

9 Event reconstruction and categorization

The first attempt for all events is the resolved reconstruction described in Section 6. If an event passes the required selection criteria of the 2t category, no further attempt of a different reconstruction is made. The same is true for 1t1l, but in these events no boosted t_h candidate must exist.

If the event is not categorized as 2t or 1t1l but an isolated lepton, at least one b jet fulfilling the tight criterion, and at least one boosted t_h candidate is found the event falls into the category BHRL (boosted t_h , resolved t_ℓ). The t_ℓ is reconstructed using the lepton and b jet for which

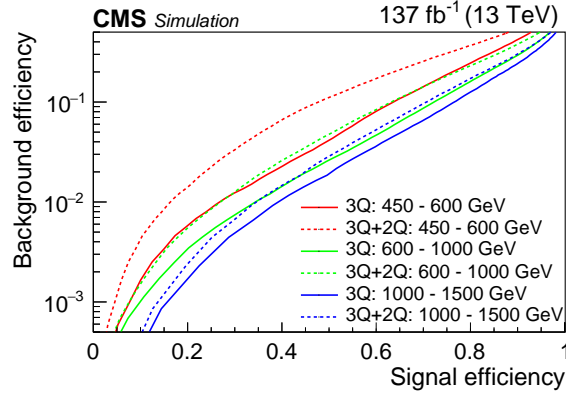


Figure 6: Background selection efficiency as function of the signal selection efficiency in various p_T regions for 3Q and 3Q+2Q jets.

$\Delta R(\ell, b \text{ jet})$ is minimal and the Neutrino-Solver finds a solution with $D_\nu < 150 \text{ GeV}$. If such a t_ℓ can be reconstructed, all t_h candidates with $\Delta R(t_h, \ell) > 1.2$ and $\Delta R(t_h, b \text{ jet}) > 1.2$, are considered. The event is filled into histograms once for each available t_h candidate. Later a fit of the H_{NN} distribution is performed to estimate the fraction correct t_h candidates.

If no isolated lepton exists, but a boosted t_ℓ with $L_{NN} > 0.7$ is found, the event is filled into histograms once for each boosted t_h candidate with $\Delta R(t_\ell, t_h) > 1.2$. We refer to this category as BHBL (boosted t_h , boosted t_ℓ). As for the BHRL category the fraction of correct t_h candidates is extracted with the fit of the H_{NN} distribution.

The category consisting of a boosted t_ℓ and a resolved t_h is not used, since a boosted reconstruction for t_h is more often needed than for t_ℓ and the fraction of these events is small. In addition, we find a low fraction of correctly reconstructed $t\bar{t}$ events in this category. Therefore, we do not use this category, but consider these events as nonreconstructable. In Fig. 7 the contributions of the various reconstruction categories as function of several kinematic variables are shown and the predicted yields are compared to the data.

10 Background subtraction in the resolved categories

In the resolved categories, 2t and 1t1l, the multijet and DY/W boson backgrounds are subtracted using combined templates of these backgrounds that are obtained from a b-jet reduced control region. In the 2t and 1t1l categories the backgrounds constitute a fraction of 1.5% and 5.5%, respectively. We repeat exactly the resolved reconstruction, but for events with the highest value of the b-tagging discriminant in a range below the usual b-tagging requirements. The exact range is optimized to obtain a good agreement between the distributions in the control region and the simulated prediction of the background in the signal region. Since the statistics of the background simulations is limited after applying all selection criteria, this can only be verified using a coarse binning as shown in Figs. 8. The edges of the discriminator range for the selection of the control region are shifted up and down so that the remaining differences between the simulated backgrounds and the distributions in the control region are covered. The distributions obtained in these varied ranges are used as shape uncertainties in background subtraction.

The normalization of this backgrounds is obtained from the comparison of data and simulation in the control region. After subtracting the predicted yield of $t\bar{t}$ events the ratio of the observed and simulated yields is used to scale the predicted event yield in the signal region.

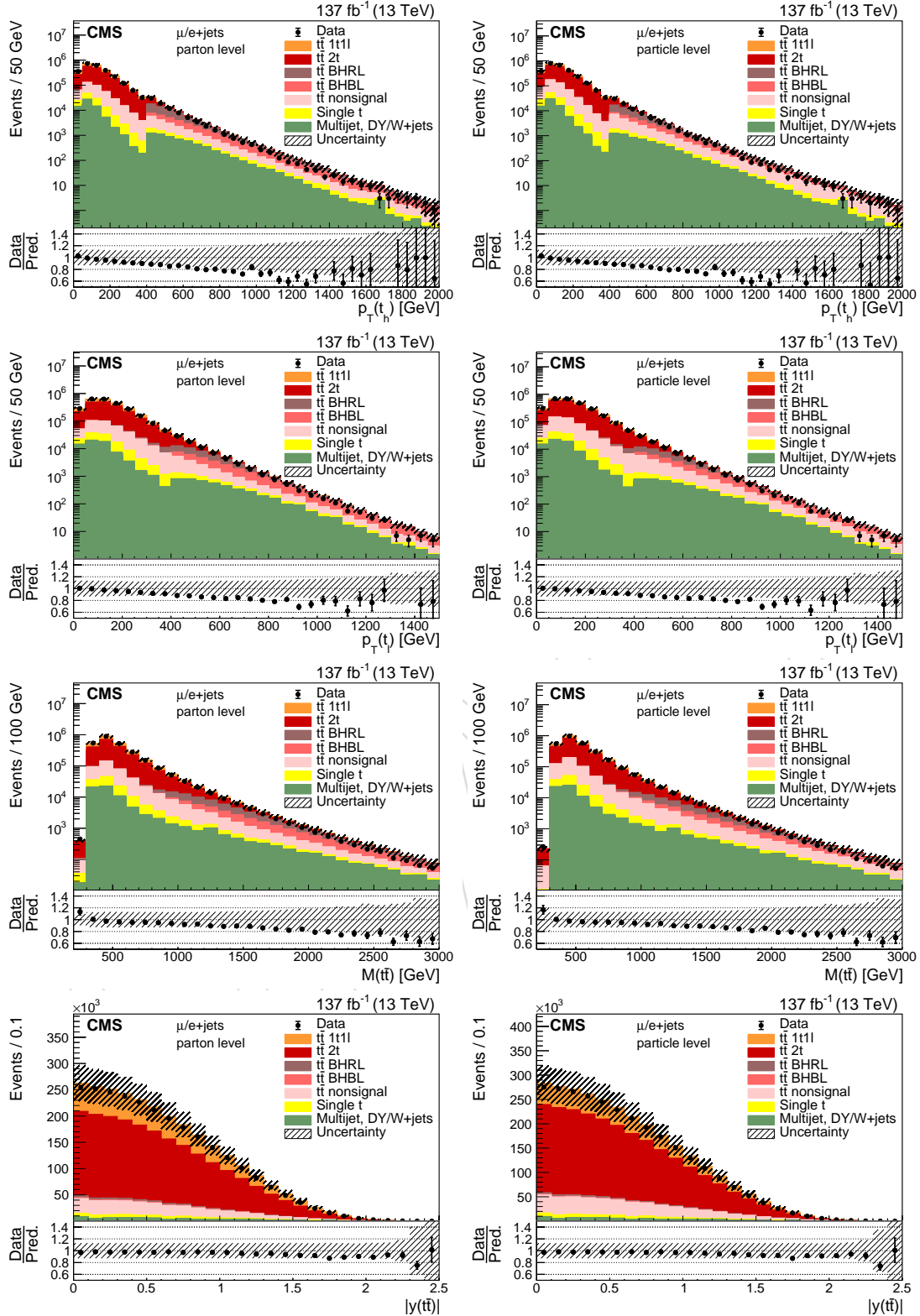


Figure 7: Contributions of the various reconstruction categories as function of several kinematic variables at detector-level. They are obtained from the POWHEG+PYTHIA8 simulation. Their yields in the electron and muon channels and in the three years are added and compared to the data. The distributions for the parton-level measurements are shown in the left and for the particle-level measurements in the right column.

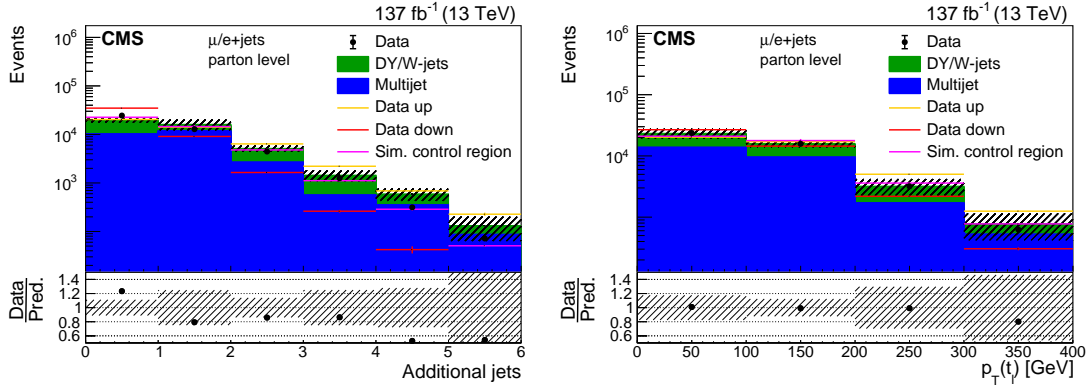


Figure 8: Comparison of the background shapes from the control region and the simulation in the signal region in the 1t1l category. The red and Orange lines show the shape uncertainties obtained by varying the selection of the control region. The magenta line is the background prediction in the control region. The hatched uncertainty shows the statistical uncertainties in the prediction.

The difference between the scale factor and one combined with the statistical uncertainty in the simulations are taken as uncertainties in the normalization of these backgrounds. This results in a normalization uncertainty of about 50%.

The obtained background predictions with their shape and normalization uncertainties are included in the fit of the cross sections as described in Section 12. Since statistical uncertainties in the simulations are dominant, the background normalization is considered as uncorrelated among the years. However, since the same method is used to derive the background distributions, the shape uncertainties are taken as correlated among the years.

Another background contribution is single top quark production which contributes about 2.5% in the 2t and 1t1l categories. It is subtracted by the cross section fits according to the SM expectations obtained from the simulation, where the following dominant uncertainties are taken into account: variations of μ_r and μ_f , jet energy scales, and b-tagging efficiency. The variations of μ_r and μ_f are treated independently from the corresponding variations of the $t\bar{t}$ simulation, while the experimental uncertainties are fully correlated among all processes.

11 Background subtraction in the boosted categories

Events with a boosted t_h , i.e., the categories BHRL and BHBL, are combined for the background subtraction. Template fits based on the distribution of H_{NN} are used to extract the yields of 3Q and 2Q events. Since the shape of H_{NN} is changing with $p_T(t_h)$, the template fit is always performed in the following bins of $p_T(t_h)$: 400, 450, 500, 550, 600, 700, 800, 900, 1000, 1500. This means in each bin of a variable under consideration we fit nine p_T bins, where not all bins are always populated. The shapes of the templates are only varied as function of $p_T(t_h)$. However, we split the templates into two regions with $|\eta(t_h)| < 0.8$ and $0.8 < |\eta(t_h)| < 1.6$. For each fitted bin the fractions in the lower and upper region are obtained from data and the templates are composed accordingly. We verified in the simulation that the templates do not depend on other properties of the events and the fitted results are unbiased.

The $t\bar{t}$ templates are taken from the simulation after applying the full event selections. Separate templates for the contribution of 2Q and 3Q events are fitted. The $t\bar{t}$ background templates contain all other selected candidates, i.e., either with a single quark pointing towards the t_h candidate or a jet not related to a t_h decay. The normalization of these three templates are free

parameters in the fit.

Single top background templates are taken from the Simulation and normalized to their SM expectation with a Gaussian prior representing the dominant normalization uncertainty of μ_T and μ_f variations, jet energy scales, and b-tagging efficiency.

The two background templates of multijet and W boson production are determined from a control region in data using events with a least one jet with $p_T > 400$ GeV and $|\eta| < 1.6$. In addition, events with an isolated electron or muon with $p_T > 15$ GeV are vetoed and there must be no boosted t_ℓ candidate with $L_{NN} > 0.7$ in the event. The contribution of all-hadronic $t\bar{t}$ events is suppressed by discarding events with more than t_h candidate with $H_{NN} > 0.4$. For the W boson template a quark jet enhanced region is needed. Therefore, we require an isolated photon with $p_T > 35$ GeV and $|\eta| < 2.4$ in the event. The additional requirement, that the photon has to be separated from all selected jets by $\Delta R(\gamma, \text{jet}) > 0.5$, increases the fraction of prompt photons. In such events we select for the template all t_h candidates that do not overlap with the photon. For the multijet template we require at least one medium b-tagged jet in the event. In such events we select for the template all t_h candidates that do not overlap with at least one of the b jets so that we obtain events with a t_h candidate and a b jet similar to the signal selection but without a lepton. In order to verify that the selected t_h candidates from the control regions provide sufficient background templates, we compare the templates obtained from the simulation in the signal region to the templates obtained from the simulation in the control region and find these in reasonable agreement. In addition, the simulation is able to describe the data in the control region.

The multijet and W boson backgrounds have slightly different shapes due to different compositions of quark flavors and gluon jets. The yields are constrained to the SM predictions using Gaussian priors with an uncertainty of 50%. These 50% uncertainties are meant to guide the fit to a minimum similar to the expectations. Since these background shapes are very similar, the obtained fraction of the background components becomes rather arbitrary if the constraints are removed. However, this does not affect the extracted signal yields, since the signal is well distinguishable from the backgrounds.

Systematic uncertainties that affect the distribution of H_{NN} in the simulation are included in the fit for the corresponding templates. These are the uncertainties in the final-state PS scale, m_t , PS tune, pileup, and energy response and resolution of the t_h candidates. These are the only sources that are expected and found to affect the substructure of jets and hence the distribution of H_{NN} . A detailed discussion of these uncertainties can be found in Section 13.

A binned maximum likelihood fit is performed simultaneously in all bins of a measurement, where the uncertainties affect the distributions of H_{NN} in all bins. The fits are performed separately for the electron and muons channels in the three years. As examples, several post-fit distributions in bins of the $p_T(t_h)$ and $M(t\bar{t})$ measurements are shown in Fig. 9.

To obtain the signal yields as a function of the variable of interest we integrate the extracted yields of Q3 and Q2 events over the $p_T(t_h)$ -bins. When the sums are calculated the correlations among the event yields as obtained from the fit are taken into account. In Fig. 10 the extracted yields are compared to the simulation. For comparison these plots also show the yields in the 2t and 1t1l categories that use the resolved reconstruction. The backgrounds in the resolved categories are subtracted using the techniques discussed in Section 10. The ratio of data to the prediction as a function of $p_T(t_h)$ shows a smooth transition between the boosted and resolved reconstruction.

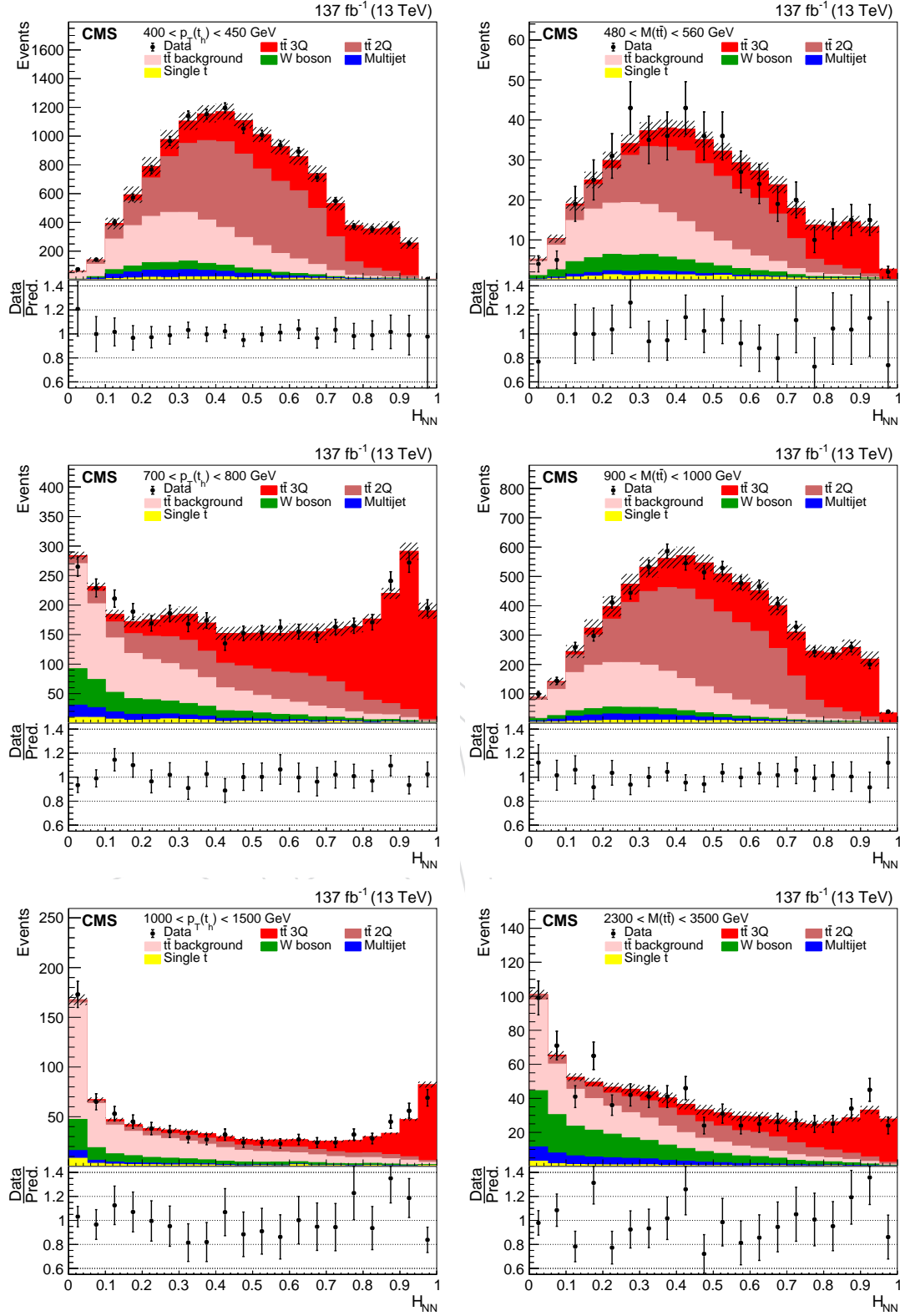


Figure 9: Post-fit distributions in bins of the $p_T(t_h)$ (left) and $M(t\bar{t})$ (right) measurements. For illustration the distributions of the electron and muon channels are added for the three years. In addition, for the $M(t\bar{t})$ measurement the results are integrated over the $p_T(t_h)$ bins that are fitted separately for each $M(t\bar{t})$ bin.

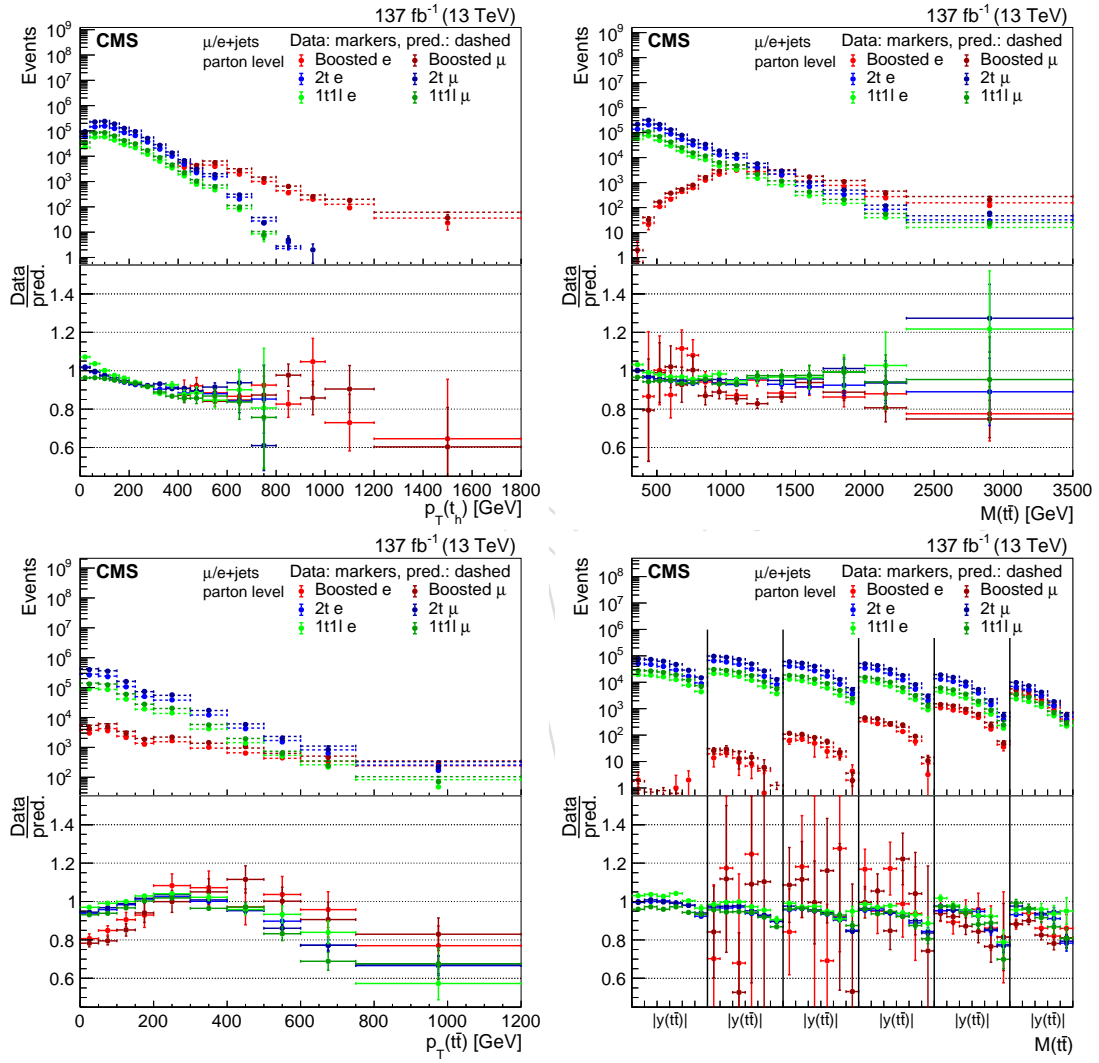


Figure 10: Signal yields in the various categories after background subtraction.

12 Extraction of the differential and inclusive cross sections

As explained in Section 11 the BHRL and BHBL categories are combined in the “boosted” category for the fit of H_{NN} in the background subtraction. The distributions in the boosted, the 2t, and the 1t1l categories are used in a fit for the extraction the differential cross sections. These three categories are further split into the electron and muon channels and are obtained for the three years. This results in 18 categories entering the fit.

For the extraction of the cross sections the response matrices R are needed. These map a vector of cross sections σ into the corresponding event yield at detector level. After adding a vector of non- $t\bar{t}$ background events b , a prediction of events at detector level is obtained that can be compared to the measured event yields

$$s = R\sigma + b. \quad (4)$$

Since non- $t\bar{t}$ backgrounds are already subtracted in the boosted category there is no b . However, $t\bar{t}$ background events exist in all categories. Because this scales with the $t\bar{t}$ cross section, its contribution is encoded in the response matrix, which can be calculated from the simulated $t\bar{t}$ events,

$$R_{ij} = \sum_m \sum_n \frac{\delta_{ni}(r_n + M_{n:})}{M_{n:}} M_{nm} \frac{\delta_{mj}}{t_m + M_{:m}} L \quad (5)$$

where $M_{n,m}$ is the two-dimensional distribution of the unfolded vs. folded quantity. The first index corresponds to a bin at the detector, the second index to a bin at the unfolded level. This distribution can only be filled if the quantity can be calculated at both levels. As abbreviations we define the quantities $M_{j:}$ and $M_{:j}$ as the sum of entries in row and column j , respectively. Events that can be reconstructed, but there is no $t\bar{t}$ pair considered as signal, are $t\bar{t}$ background events and filled into distribution r . The first ratio in Eq. 5 corrects for these non-signal $t\bar{t}$ events. Events with a signal $t\bar{t}$ pair at unfolded, but no $t\bar{t}$ pair at detector level, are filled into distribution t entering the second ratio in Eq. 5 that represents the losses due to inefficiencies and acceptance. To convert cross sections into event yields the expression is multiplied by the luminosity L . In this analysis the same binning is used at the detector and unfolded levels. In Fig. 11 we show the response matrix of the $p_T(t_h)$ measurement together with its purity (fraction of correctly reconstructed events per bin at detector level) and stability (fraction of correctly reconstructed events per bin at unfolded level). The plotted matrices show the sum of the matrices in the individual categories. Very similar reconstruction performances are expected for the three years.

With the vector of measured event yields m we define the likelihood

$$\chi^2(\sigma, v) = \sum_y \sum_c \sum_\ell (m_{ycl} - s_{ycl}((\sigma, v)))^T C_{ycl}^{-1} (m_{ycl} - s_{ycl}(\sigma, v)) + v^T Q^{-1} v, \quad (6)$$

where we sum over the years ($y = 2016, 2017, 2018$), the reconstruction categories ($c = \text{boosted}, 2t, 1t1l$), and the lepton channels ($\ell = e, \mu$). In the resolved categories the covariance matrix C is a diagonal matrix with the numbers of observed events per bin, while in the boosted categories, since the background was already subtracted, the covariance matrix is obtained from the fits as described in Section 11. In each category only bins with at least four events are used, i.e., very low and unpopulated bins are not taken into account for the fit. For such bins the χ^2 fit is

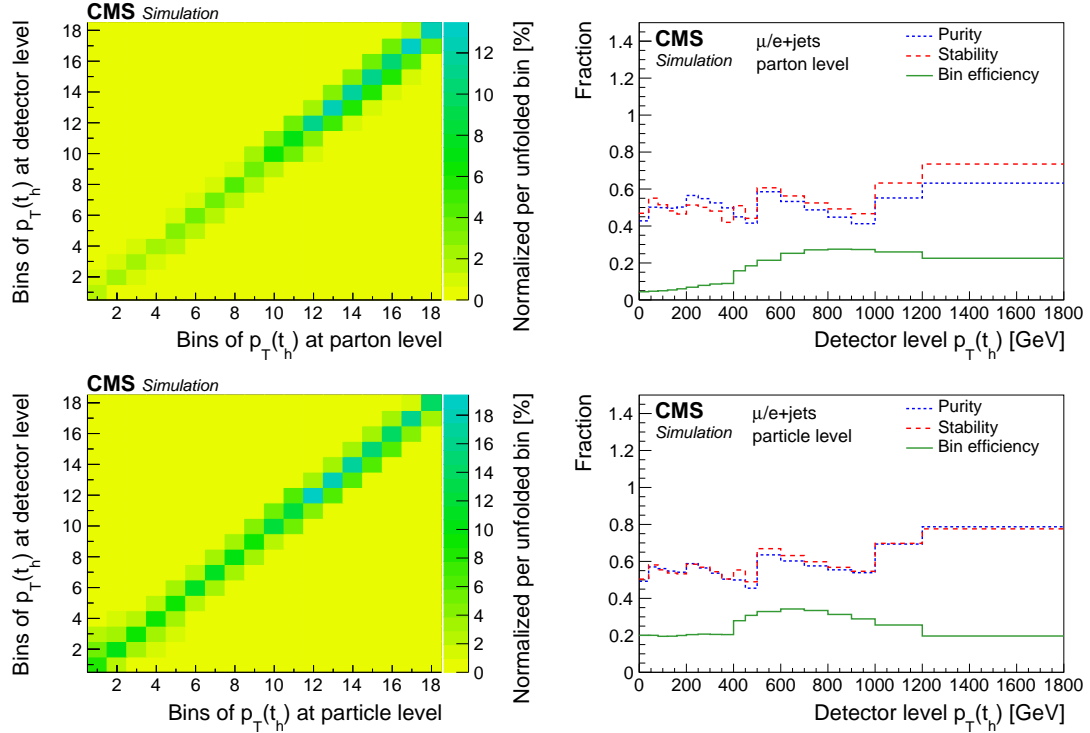


Figure 11: Sum of response matrices of the $p_T(t_h)$ measurements together with their purity, stability, and the efficiency per bin.

not well defined. However, since the combined event yields of all categories is at least several 100–1000 events per bin, neglecting such a few events does not affect the results. The number of degrees of freedom of the fit is given by the number of bins taken into account minus the number of bins in σ .

The predicted event yields depend on the differential cross section and the systematic uncertainties parameterized as function of nuisances ν . The later are constrained by the last term, where the matrix Q is the correlations matrix of the nuisance parameters. Especially, the correlations of the uncertainty sources between the data from different years are important. They are discussed in detail in Section 13. The goodness of the fit is calculated from the minimized χ^2 and the number of degrees of freedoms. The corresponding p -values, shown in Fig. 12, are reasonable and none of the p -values is below 1%.

13 Systematic uncertainties

In the fits of the cross sections several sources of uncertainties affect the response matrix. These sources can be split into main categories of theoretical and experimental uncertainties. Theoretical uncertainties are:

- The effects of higher order contributions to the cross section calculations are estimated by varying μ_r and μ_f separately by a factor of two. Distributions for these variations are obtained using event weights in the POWHEG+PYTHIA8 simulation. The two scale variations are included as two separate uncertainties in the fit. Since the POWHEG calculation is the same in all three years, these uncertainties are taken as fully correlated.
- Since the μ_r and μ_f variations barely describe the differences in the shape of the p_T

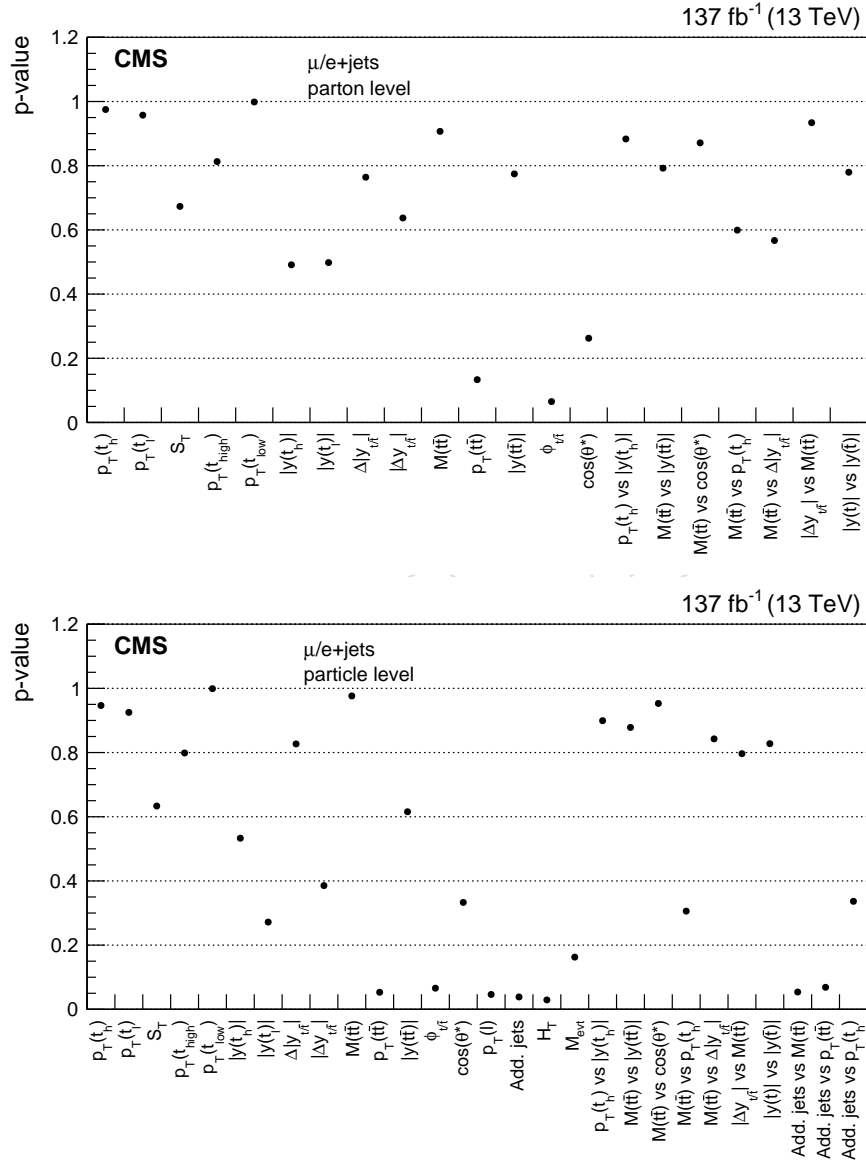


Figure 12: The p -values of the χ^2 fits are shown for the parton- (upper) and particle- (lower) level measurements.

spectrum in POWHEG at NLO and MATRIX at NNLO precision an additional uncertainty is introduced, where the variation of this uncertainty corresponds to a reweighting of the top quark p_T distribution in the POWHEG+PYTHIA8 simulation to the spectrum from MATRIX. This uncertainty is correlated among the data from the three years.

- With NNPDF30_nlo_as_0118 in the CUETP8M2T4 tune and NNPDF31_nnlo_hessian_pdfas in the CP5 tune different PDFs are used. For each PDF 100 nuisances are added to the fit that scale the uncertainty variations. In addition, a variation of α_s by 0.002 in the PDF fit is taken into account. The distributions are obtained using the corresponding event weights. Only 2017 and 2018 are correlated, while 2016 is taken as uncorrelated.
- The uncertainty in the initial-state PS is estimated by varying the shower scale by a factor of two. The corresponding distributions are obtained using event weights. With $\alpha_s = 0.1108/0.118$ for T4/CP5 the values are very similar and we assume that this uncertainty is fully correlated among the years.
- The uncertainty in the final-state PS is estimated by varying the shower scale by a factor of 2. The corresponding distributions are obtained using event weights. With 0.1365/0.118 for T4/CP5 for T4/CP5 the values are different and we assume that this uncertainty is uncorrelated for the two tunes.
- In POWHEG the matching between the matrix element calculation and the parton shower is controlled by the parameter h_{damp} . The values used with the CUETP8M2T4 and CP5 tunes are $1.38^{+0.92}_{-0.51}$ and $1.58^{+0.66}_{-0.59} m_t$, respectively. Since the values are similar, the uncertainty is taken as fully correlated among the data from different years. Separate samples produced with the different values of h_{damp} are used to obtain the corresponding distributions.
- Separate samples produced with $m_t = 171.5$ and $m_t = 173.5$ are used to estimate the uncertainty due to the uncertainty in m_t . This 1 GeV variation is fully correlated among the data from different years.
- The uncertainty in the hadronization is estimated using separate samples that represent an envelope of the uncertainties in the tuning. This uncertainty is fully correlated between 2017 and 2018, but taken as uncorrelated with the different tune in 2016.
- The fraction of leptonically decaying B hadrons is changed according to the known precision of the branching fraction using event based reweighting. This uncertainty is fully correlated among the data from different years.
- The uncertainty in the color reconnection is assessed using an alternative model where the reconnection of colored particles from resonant decays is activated in PYTHIA8, while this is deactivated in the default setup. The difference between these two is taken as symmetric uncertainty. We assume that the amount of color reconnection is fully correlated among the data from the three years.

Experimental uncertainties are:

- The uncertainties in the luminosity are 2.5%, 2.3%, and 2.5% for 2016, 2017, and 2018, respectively. Their correlations are evaluated to be between 20% and 30% [51–53]. These uncertainties and their correlation are directly used in the cross sections fit.
- The uncertainty in the pileup estimation can be divided into two sources: the uncer-

tainty in the inelastic cross section of about 4.5% [54] and the uncertainty in the instantaneous luminosities. Since the former is dominant and fully correlated among the years, a high correlation of about 85% among the years is expected. Response matrices for enhanced and reduced pileup are obtained by reweighting the distribution of the number of pileup interactions in the simulation.

- The jet energy scale uncertainty is split into 20 different sources that are relevant for jets within the tracker acceptance. The correlation among the years is evaluated for each source. The sources affect the ordinary jets and PUPPI jets simultaneously, but in different ways. The differences in the response matrices are obtained by rescaling the jet momenta in the simulation.
- For ordinary jets and PUPPI jets separate uncertainties in the energy resolutions are introduced, because the different methods of pileup corrections have large effects on the resolutions. The uncertainties taken as uncorrelated among the years. The response matrices for different jet resolutions are obtained by rescaling the jet resolution in the simulation.
- The dominant source of uncertainty in the p_T^{miss} is the uncertainty in the jet energy calibration. Therefore, the p_T^{miss} is also recalculated whenever the jet momenta are rescaled to evaluate their uncertainties. An additional contribution to the uncertainty due to PF particles that do not belong the selected jets is estimated. A 50% correlation among the years is assumed for this uncertainty.
- For electrons and for muons an uncertainty in the trigger efficiency and in the reconstruction efficiency are considered. Since the same methods for measuring these efficiencies in data are used in all years, there might be a common bias and we assume a correlation of 50% among the years.
- Uncertainties in the tagging and mistagging efficiencies of various b-tagging requirements have been studied [48], where the tagging efficiency is the efficiency for b jets to fulfill a criterion, while the mistagging efficiency refers to all other jets. In this analysis a tight and loose b-tagging requirement are used. To simulate the variations of the efficiencies, event weights are calculated according to the probability to find the combination of tagged, nontagged, mistagged, and nonmistagged jets under the assumption of altered efficiencies. We alter separately the efficiencies of the loose and tight requirements and in addition the efficiency of passing the loose but not the tight requirement. Each of the three variations introduces a parameter of the tagging and mistagging efficiencies. We assume a 50% correlation among the years.

In addition, we estimate the effect of the limited statistics in the simulations by repeating the whole fit 100 times with varied response matrices. From these results we calculate the covariance matrix, which is added to the covariance matrix of the other uncertainties as obtained from the fit with the default response matrices. The response matrices are varied randomly taking into account statistical uncertainties in the default POWHEG+PYTHIA8 simulation and in the simulations used for the uncertainty estimations of m_t , h_{damp} , and PS tune. For the uncertainties estimated based on event weights or rescaling of object momenta the correlations between the default bin contents and the altered bin contents are taken into account when the random variations are generated. Overall, the uncertainty due to limited statistics in the simulations is of moderate size similar to other leading systematic uncertainties. It becomes a dominant systematic only in a few bins, but it is always small compared to the statistical uncertainty in data.

In Fig. 13 the uncertainties in the measurements of a few differential cross sections are shown

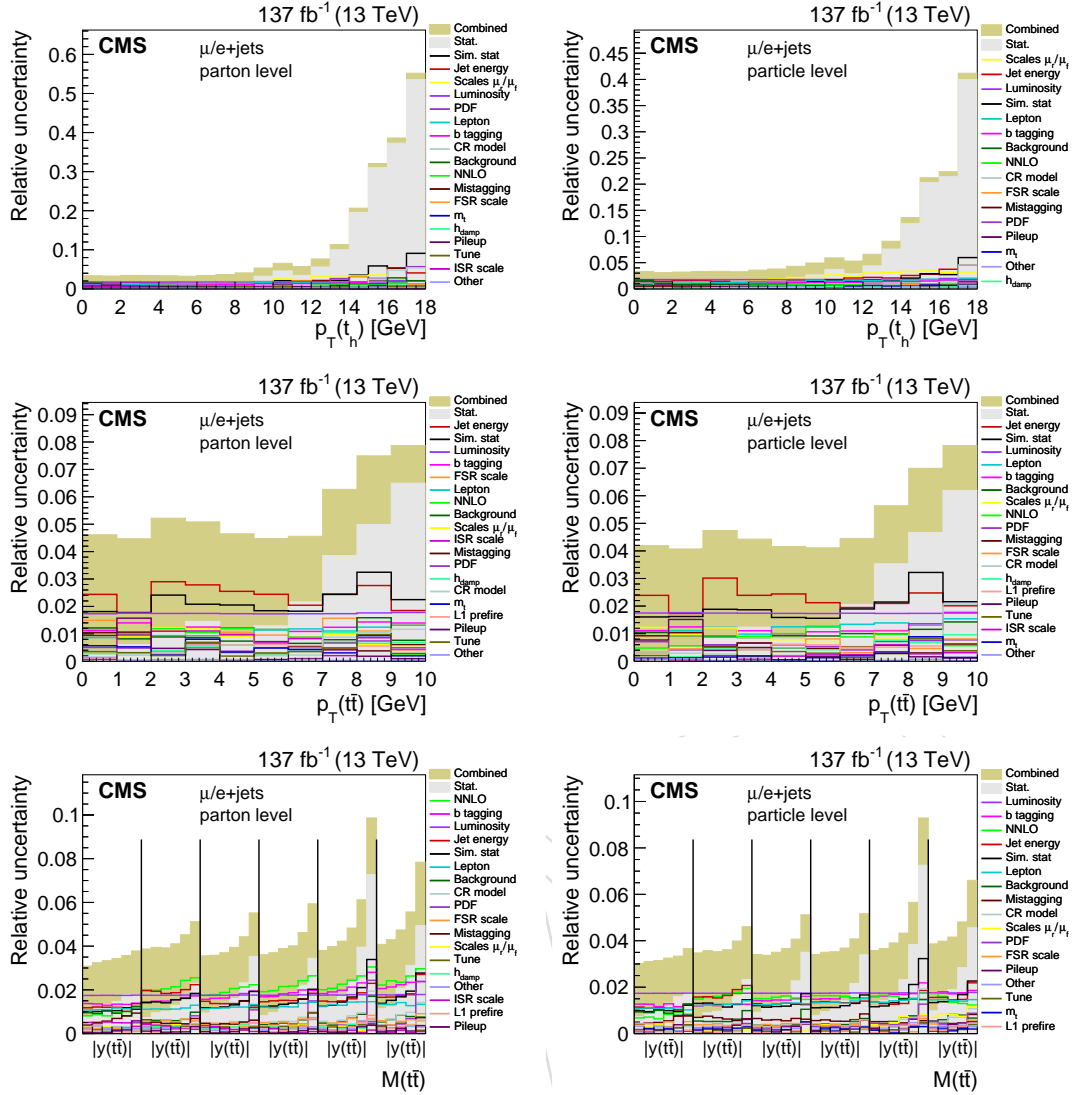


Figure 13: Uncertainties split into various sources for three exemplary distributions. Uncertainties in the parton-level measurement are shown on the left and in the particle-level measurement on the right.

and split into individual sources. The statistical uncertainty in data becomes dominant only in the tails of the distributions, while the bulk is dominated by systematic uncertainties. The main contributions are from the uncertainty in the jet energy scale and luminosity. The leading theoretical uncertainties are the variations of μ_r , μ_f , and the uncertainty that reflects the difference in $p_T(t)$ between the NLO and NNLO calculations.

14 Results at parton and particle level

In Fig. 14 the results of χ^2 tests comparing the measurements with several predictions are shown. For the comparison the covariance matrices of the measurements and of the predictions are taken into account. For the POWHEG+PYTHIA8 simulations all theoretical uncertainties for MATRIX only the scale uncertainties are considered. The individual uncertainty sources are assumed to be correlated among the bins, while the sources themselves are uncorrelated. Most of the distributions are well described by the three predictions, where it should be noted that the

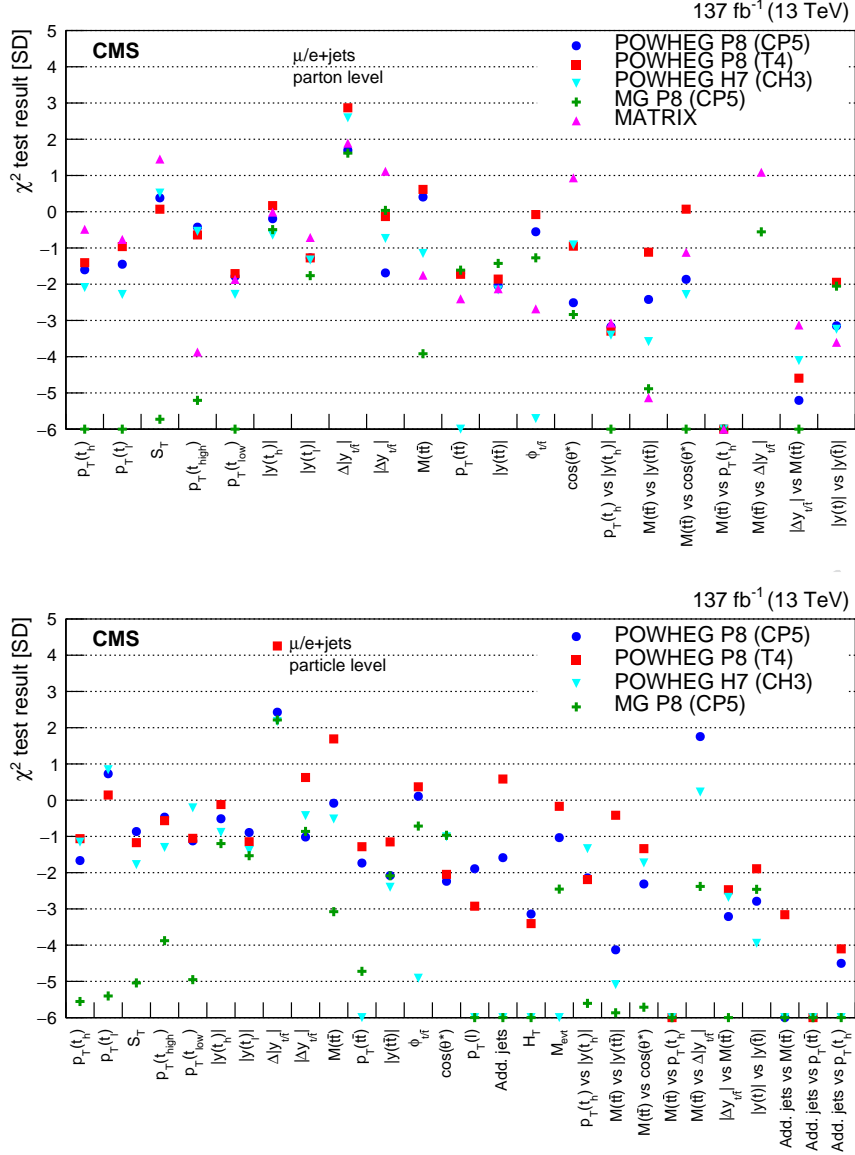


Figure 14: Results of χ^2 tests in standard deviation (SD) comparing the measured cross sections parton (upper) and particle (lower) level to various predictions. The uncertainties in the measurements and the predictions are taken into account.

uncertainty in the MATRIX calculation is significantly smaller than in the POWHEG+PYTHIA8 predictions. We observe a deficit at high $|y(t\bar{t})|$. This is visible in the χ^2 -test results. Especially, the double differential cross section of $M(t\bar{t})$ vs. $|y(t\bar{t})|$ has a low compatibility with all predictions. Other distributions that are not described by the tested predictions are $|\Delta y_{t/\bar{t}}|$ vs. $M(t\bar{t})$ and $M(t\bar{t})$ vs. $p_T(t_h)$. In addition, at particle level the kinematic distributions in bins of jet multiplicity are not well described. This could be understood since with POWHEG+PYTHIA8 the higher multiplicities of additional jets are only predicted by the PS.

The differential cross sections as function of $p_T(t_h)$, $p_T(t_\ell)$, $p_T(t_{\text{high}})$, $p_T(t_{\text{low}})$, and S_T are presented in Figs. 15 and 16 and compared to the POWHEG and the MATRIX predictions. The p_T spectra are softer than predicted by POWHEG. Such a deficit in data of up to 20% at $p_T > 500$ GeV confirms previous measurements. However, the NNLO QCD calculation performed with MATRIX seems to describe the data significantly better with the exception of $p_T(t_{\text{low}})$. As

discussed in [33] $p_T(t_{\text{high}})$ and $p_T(t_{\text{low}})$ cannot be accurately described by fixed order calculations but by all-order resummation effects of Sudakov type have to be taken into account.

Figures 17 and 18 show the rapidities $|y(t_h)|$, $|y(t_\ell)|$, and the differences $\Delta|y_{t/\bar{t}}|$ and $|\Delta y_{t/\bar{t}}|$. They are all well described by the simulations. Only a small tendency towards higher values is observed for $\Delta|y_{t/\bar{t}}|$.

In Figs. 19 and 20 the differential cross sections are shown as functions of kinematics of the $t\bar{t}$ system $M(t\bar{t})$, $p_T(t\bar{t})$, $|y(t\bar{t})|$, $\Delta\phi_{t/\bar{t}}$, and $\cos(\theta^*)$. Especially the POWHEG+PYTHIA8 samples predict a harder spectrum of $p_T(t\bar{t})$. A discrepancy is found at high values of $|y(t\bar{t})|$, where all calculations predict higher cross section than observed.

The double differential cross sections are shown in Figs. 21–34. The distribution of $p_T(t_h)$ vs. $|y(t_h)|$ shown in Figs. 21 and 22 is reasonably described by all predictions. Only the deficit in the high $p_T(t_h)$ bins becomes visible for the NLO calculations.

As mentioned earlier and shown in Figs. 23 and 24, we observe a deficit at high rapidities in the $M(t\bar{t})$ vs. $|y(t\bar{t})|$ measurements, where the effect seems more pronounced at higher $M(t\bar{t})$.

In Figs. 25 and 26 the measurement of $M(t\bar{t})$ vs. $\cos(\theta^*)$ is shown. The NLO calculations seem to predict a more flat distribution than observed. With the NNLO calculation of MATRIX the behavior is described better.

The measurement of $M(t\bar{t})$ vs. $p_T(t_h)$, shown in Figs. 27 and 28, is not well described by any of the predictions. While the measured p_T spectrum is in agreement or even harder than predicted at low $M(t\bar{t})$, the spectrum is softer at high $M(t\bar{t})$. The χ^2 tests confirm the incompatibility of this measurement and the tested predictions.

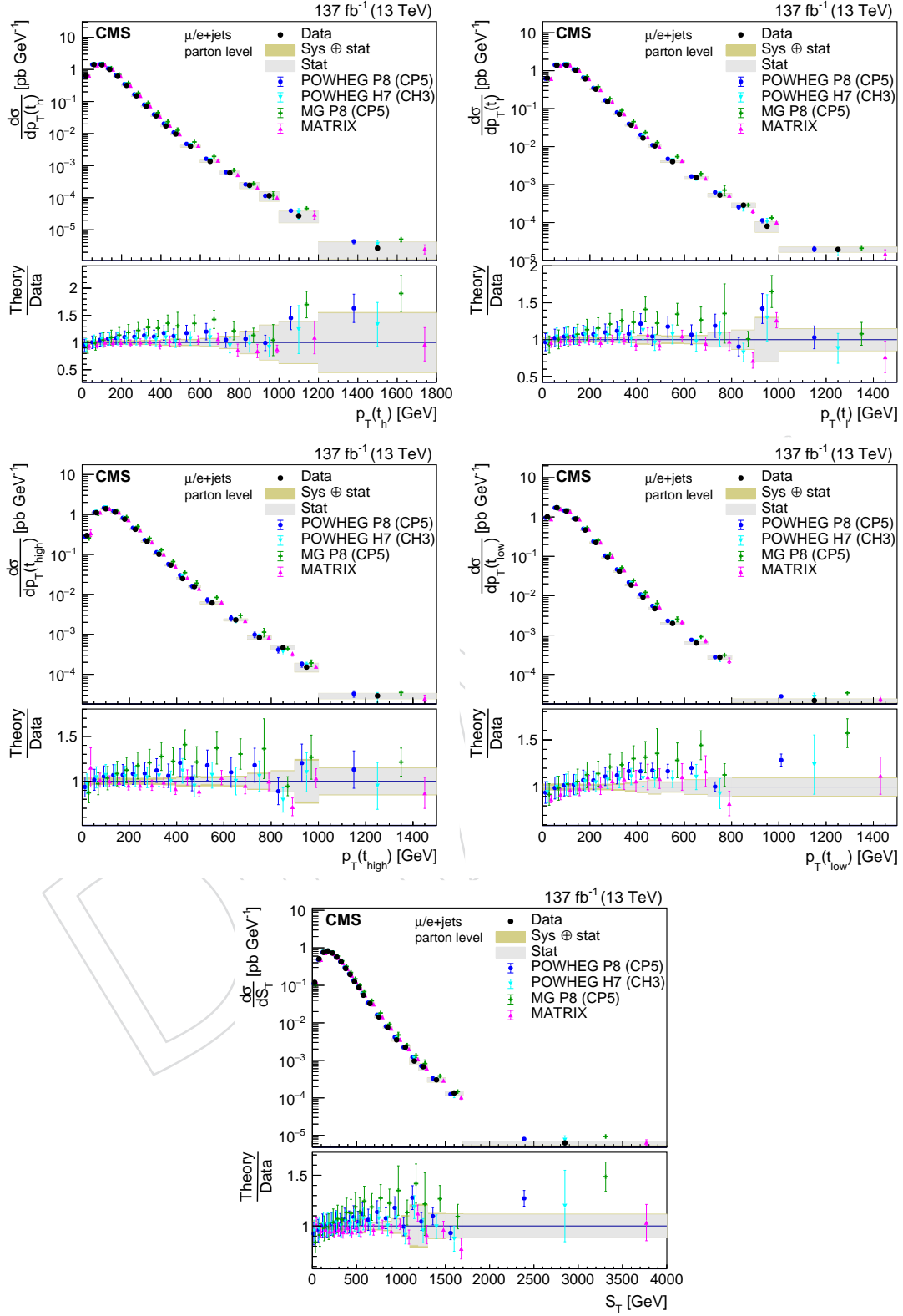
The measurement of $|\Delta y_{t/\bar{t}}|$ vs. $M(t\bar{t})$ is shown in Figs. 29 and 30. This distribution is known to be sensitive to electroweak corrections, especially to the top quark Yukawa coupling [55]. The NNLO calculation results in an improved description of this distribution.

In Figs. 31 and 32 the measurements of $M(t\bar{t})$ vs. $\Delta|y_{t/\bar{t}}|$ are shown. Especially, at low $M(t\bar{t})$ the NLO calculations predict a distribution peaking stronger at zero. In general, we would warn to use these measurements of $\Delta|y_{t/\bar{t}}|$ to extract information about the charge asymmetry, since a significant effect of the asymmetry in this measurements is introduced by the acceptance corrections.

In Figs. 33 and 34 the double differential cross section as function of $|y(t)|$ vs. $|y(\bar{t})|$ are shown. This can be used to calculate the ratio of cross sections of t and \bar{t} as function of rapidity taking into account bin-by-bin correlations correctly. Differences in the rapidity of t and \bar{t} are a direct consequence of the charge asymmetry in $t\bar{t}$ production in pp collisions, where in average $|y(t)|$ is higher than $|y(\bar{t})|$. In contrast to measurements based on $\Delta|y_{t/\bar{t}}|$ the acceptance correction of this double differential measurement does not depend on the asymmetry in the simulation. However, no significant difference in $|y(t)|$ and $|y(\bar{t})|$ is observed. The simulation shows that the main effect of the charge asymmetry is expected at high rapidities, where the measurement is limited by statistics and detector acceptance.

The integrated differential cross sections at parton level correspond to the $t\bar{t}$ production cross section in the e/μ +jets channel. Only for rapidity related distributions an overflow of up to 3% is estimated from the simulation. This is corrected for the cross sections obtained for the different measurements shown in Fig. 35.

All cross section values are similar though it is difficult to judge their agreements because they do not represent independent measurements. The most precise measurement is obtained from

Figure 15: Differential cross section as functions of $p_T(t_h)$, $p_T(t_\ell)$, $p_T(t_{\text{high}})$, $p_T(t_{\text{low}})$, and S_T

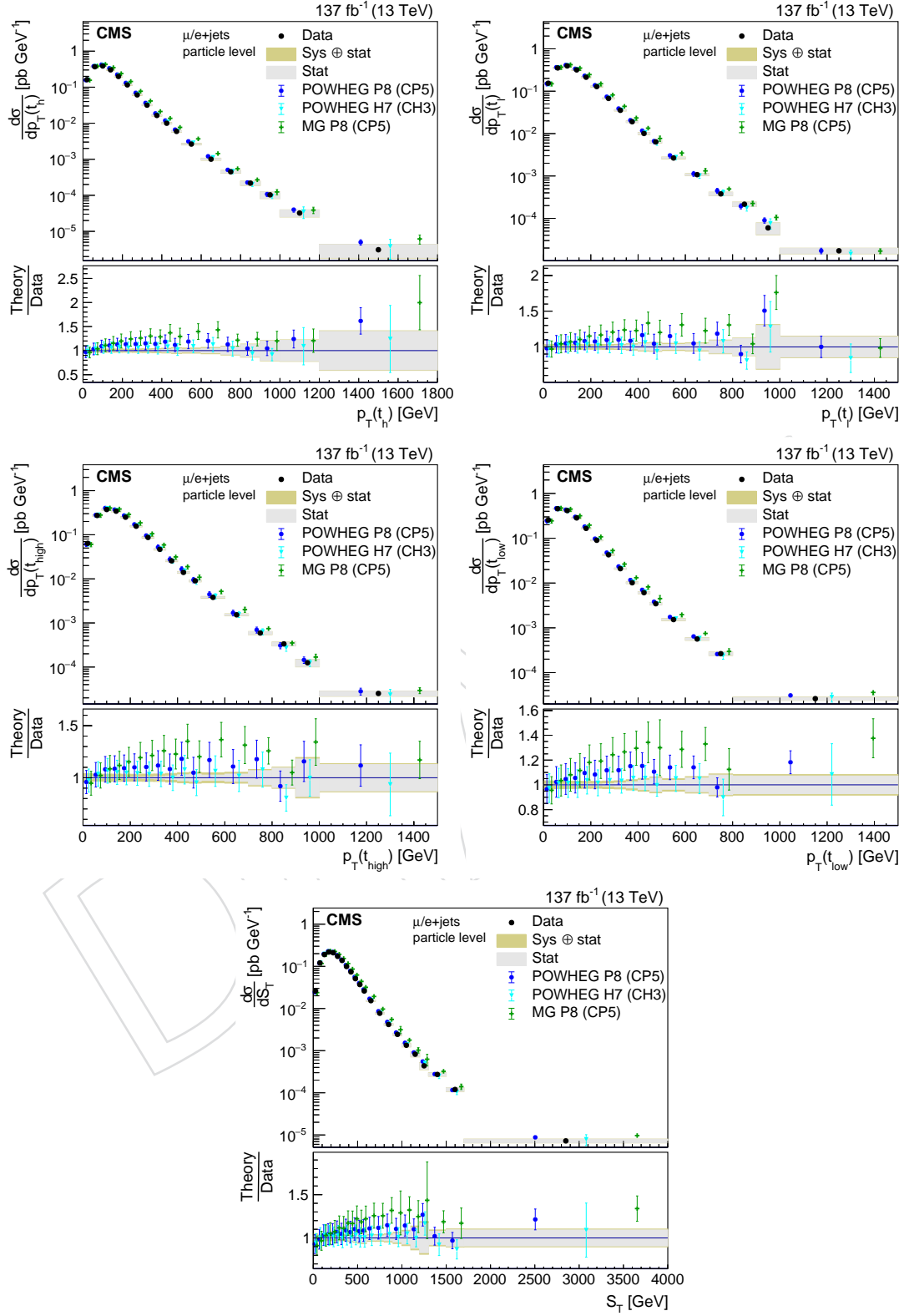


Figure 16: Differential cross section as functions of $p_T(t_h)$, $p_T(t_l)$, $p_T(t_{\text{high}})$, $p_T(t_{\text{low}})$, and S_T

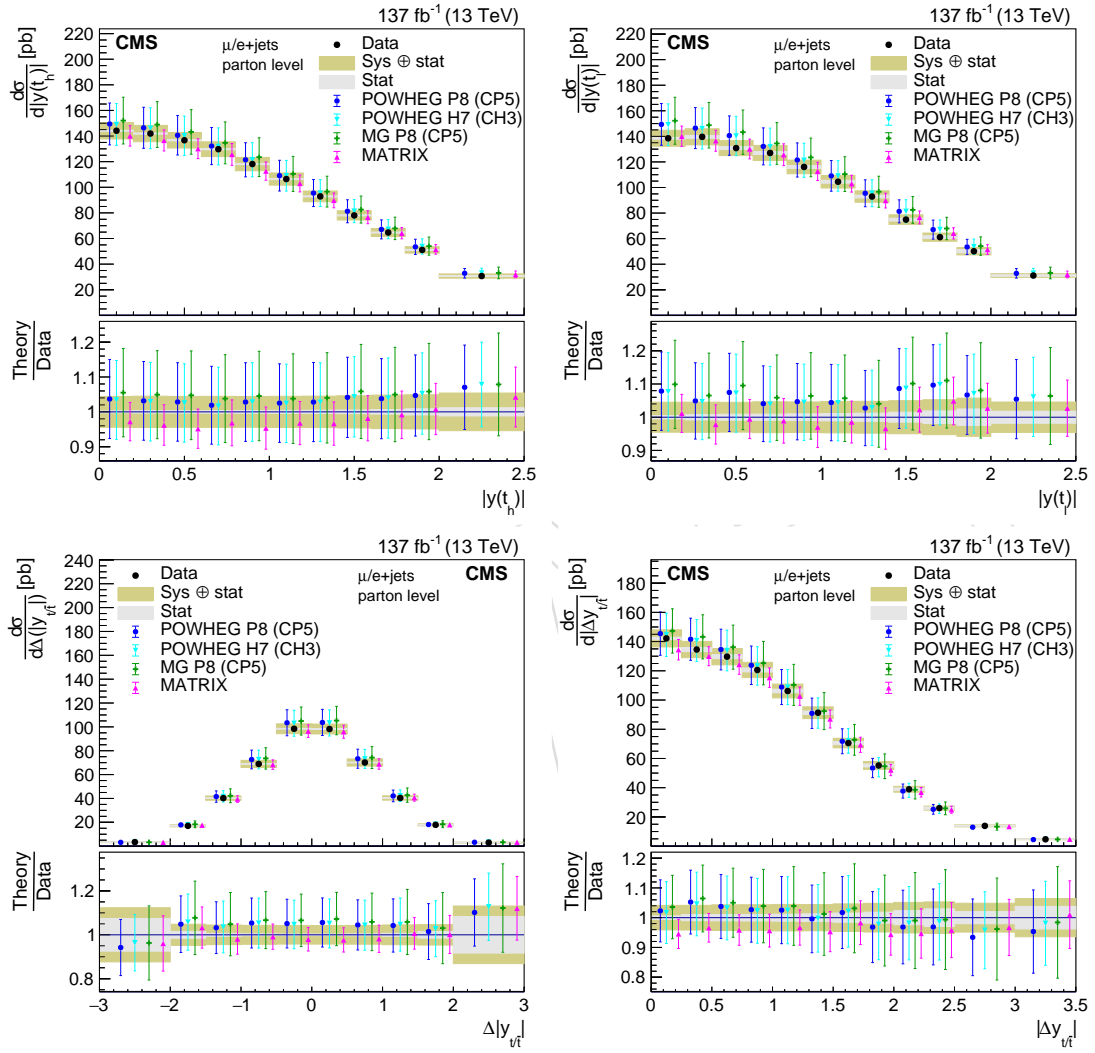


Figure 17: Differential cross section as function of $|y(t_h)|$, $|y(t_\ell)|$, and the differences $\Delta|y_{t/\bar{t}}|$ and $|\Delta y_{t/\bar{t}}|$.

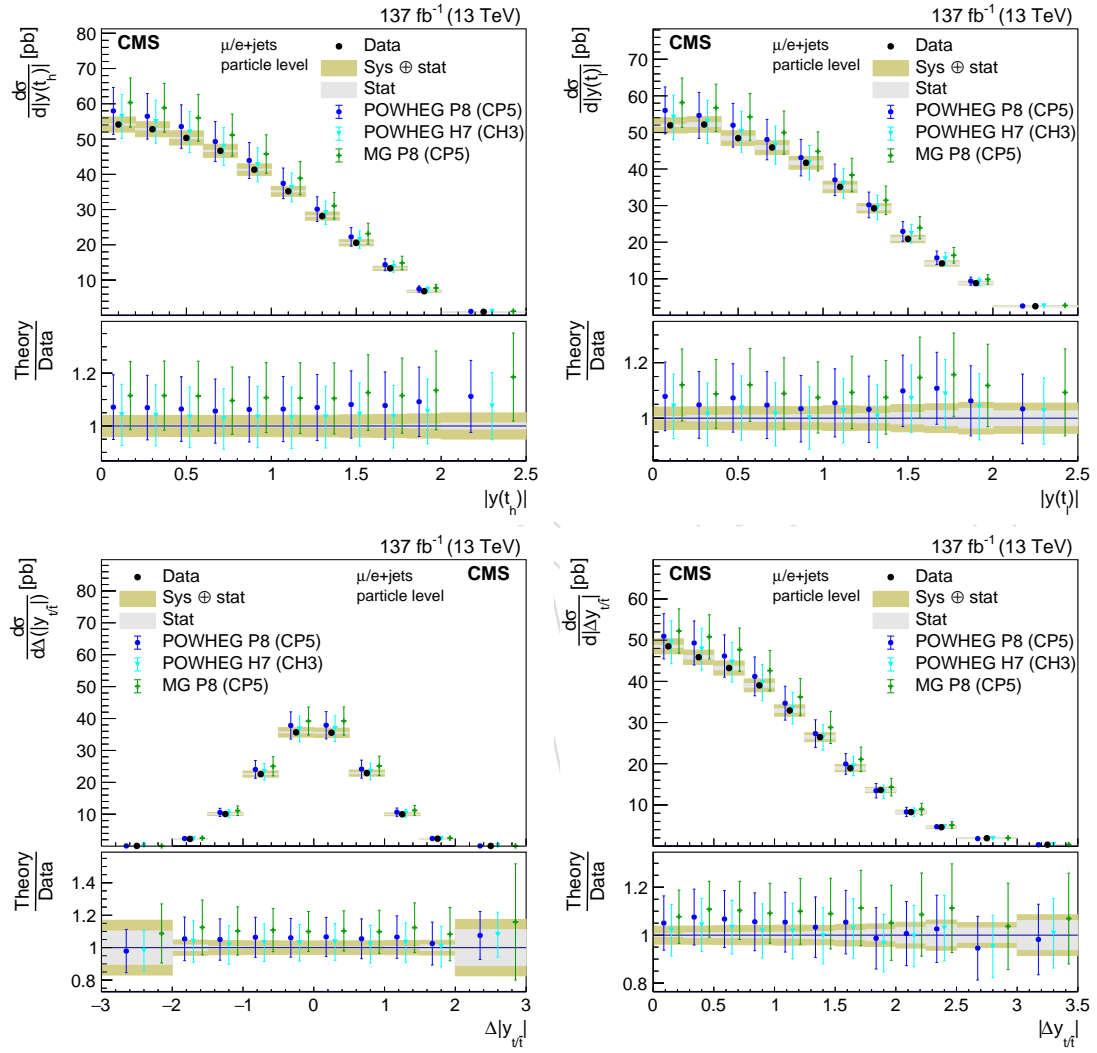
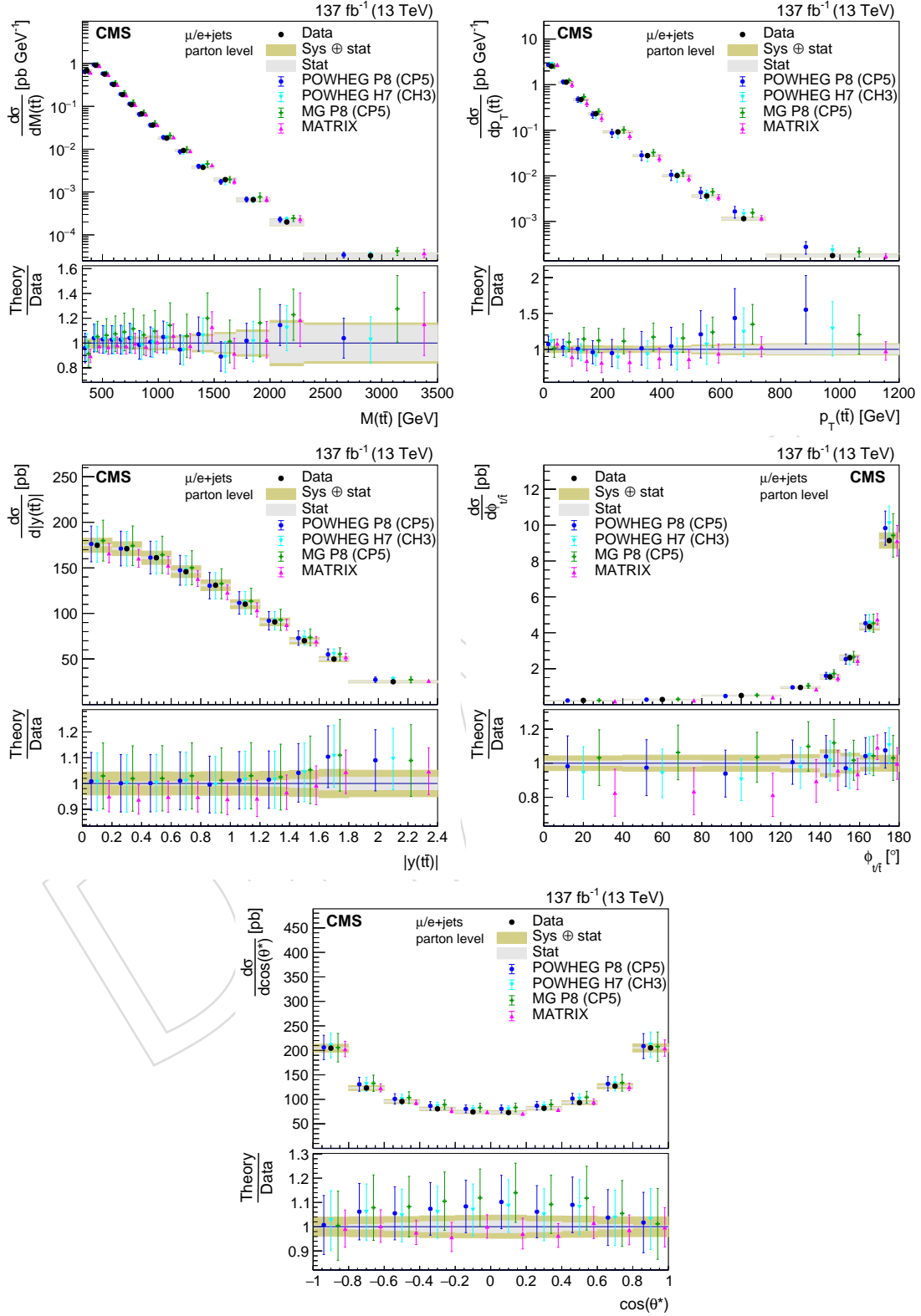
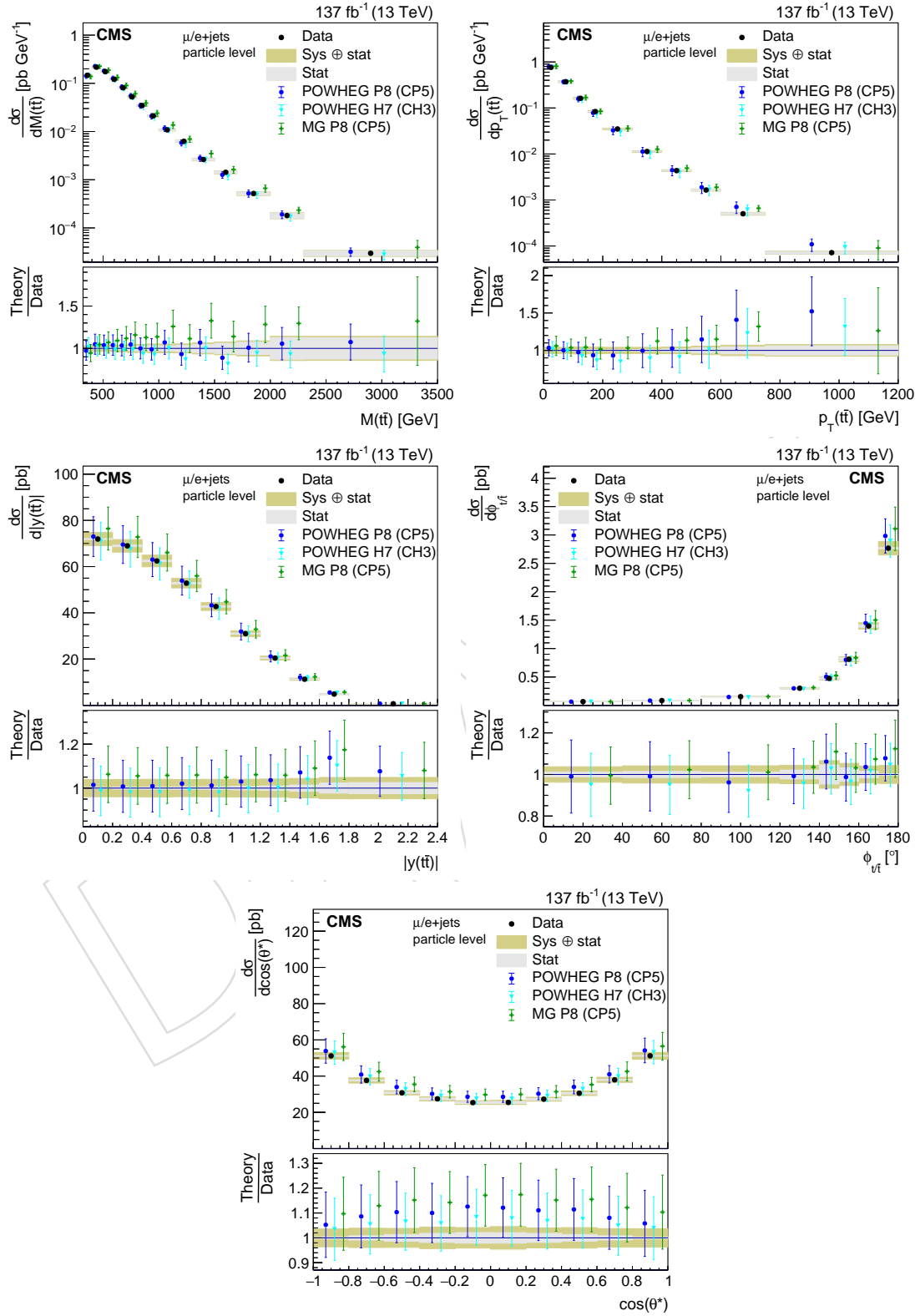
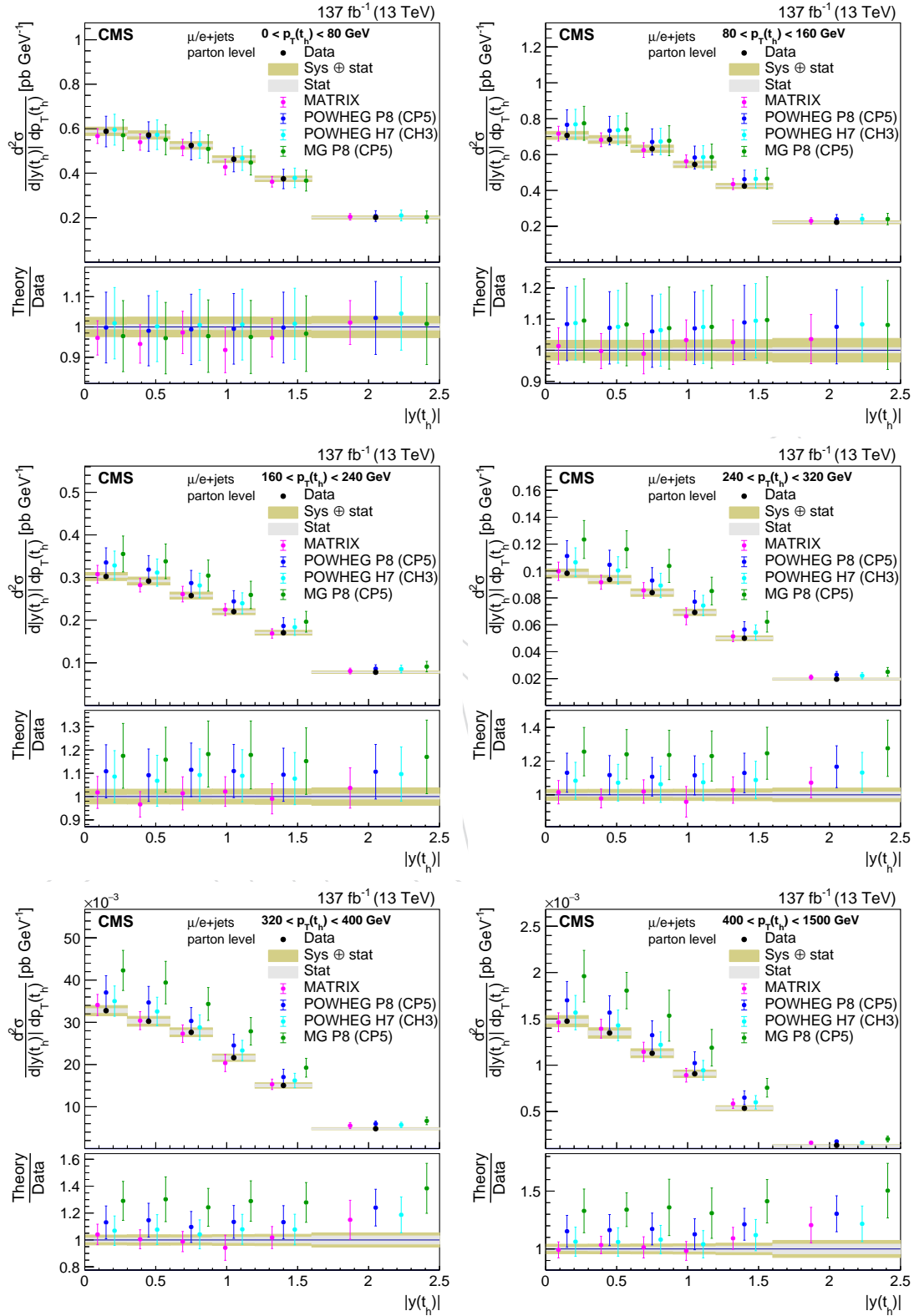


Figure 18: Differential cross section as function of $|y(t_h)|$, $|y(t_l)|$, and the differences $\Delta|y_{t/\bar{t}}|$ and $|\Delta y_{t/\bar{t}}|$.

Figure 19: Differential cross sections as functions of quantities of the $t\bar{t}$ system.

Figure 20: Differential cross sections as functions of quantities of the $t\bar{t}$ system.

Figure 21: Double differential cross section as function of $p_T(t_h)$ vs. $|y(t_h)|$.

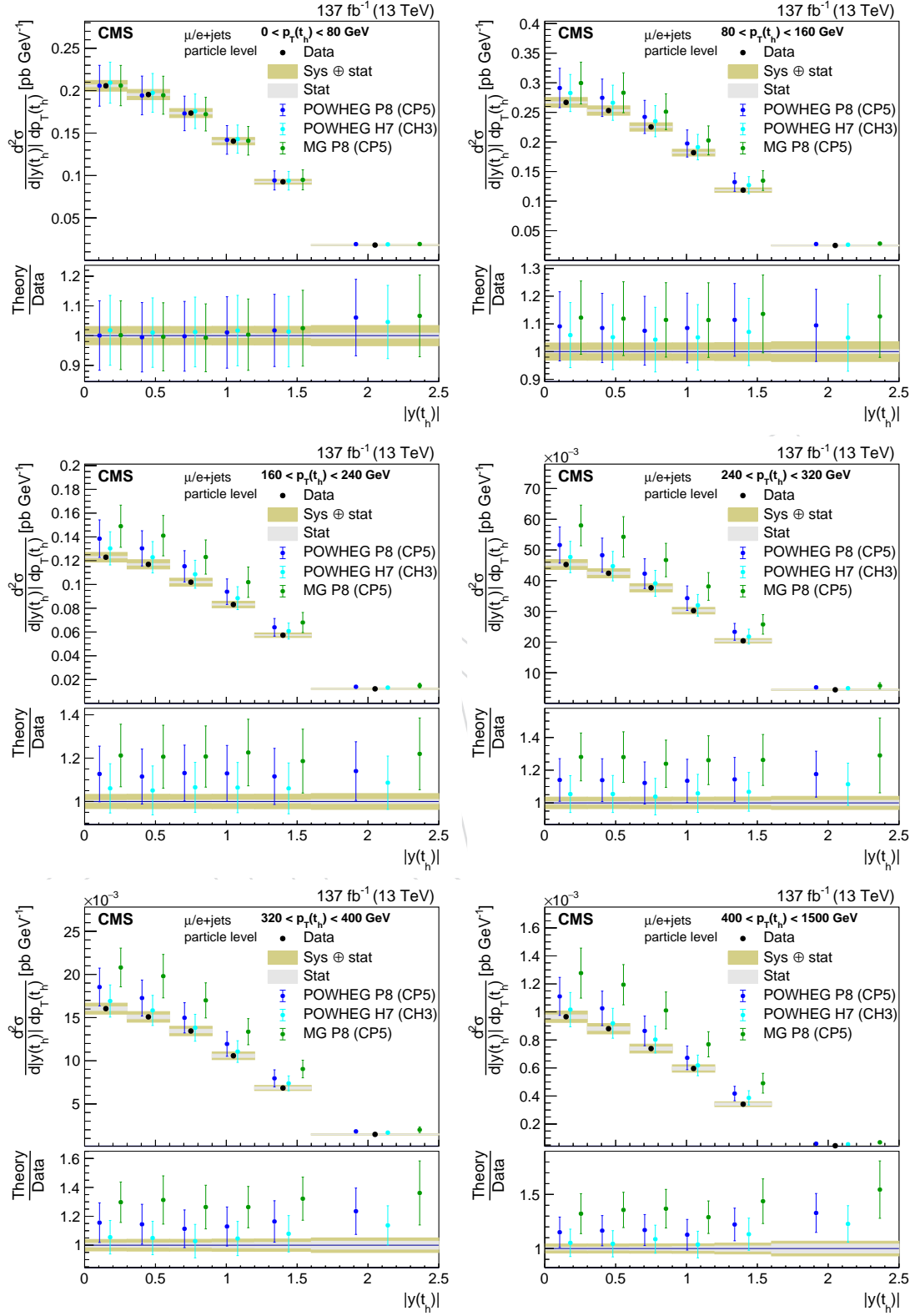
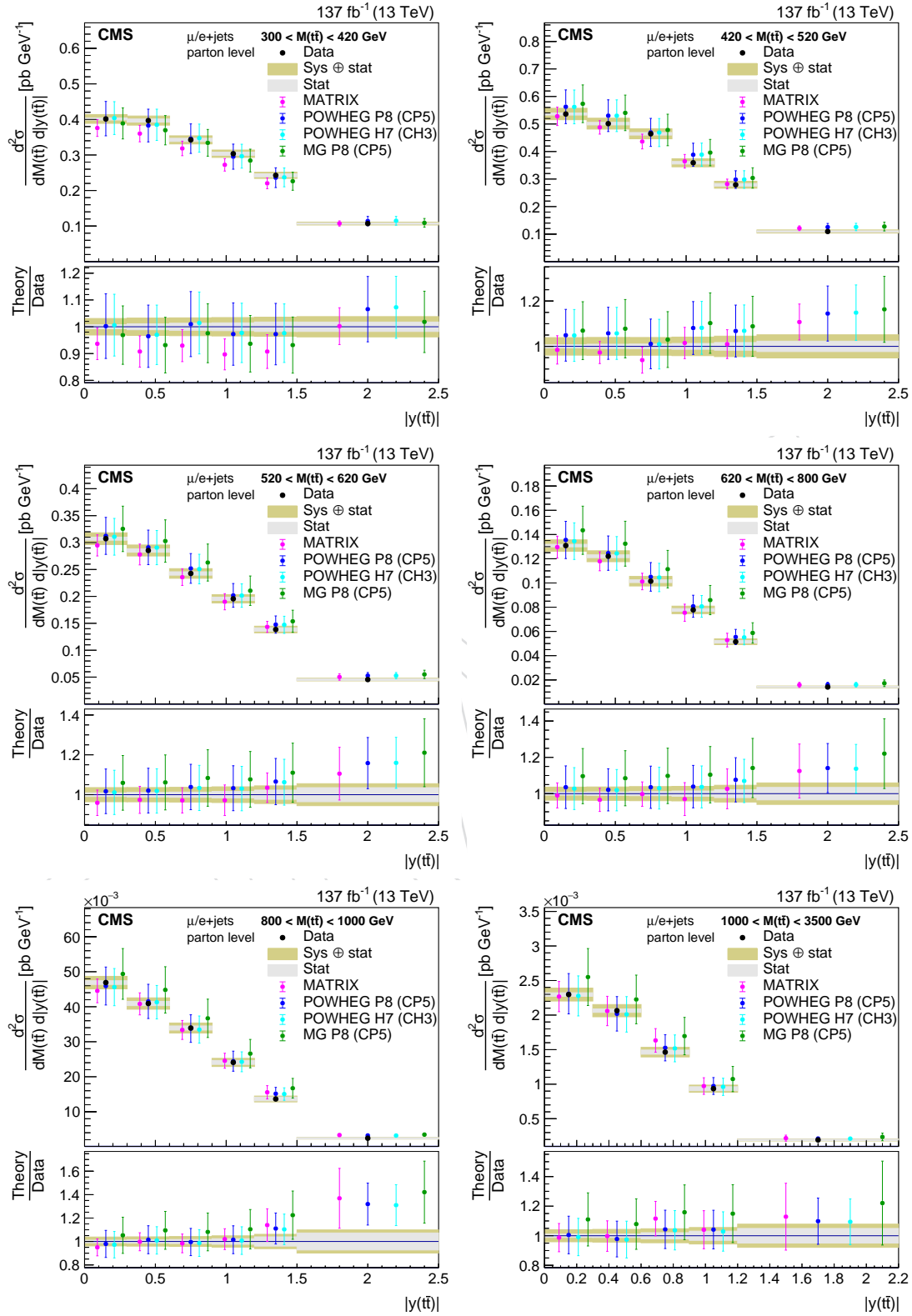


Figure 22: Double differential cross section as function of $p_T(t_h)$ vs. $|y(t_h)|$.

Figure 23: Double differential cross section as function of $M(t\bar{t})$ vs. $|y(t\bar{t})|$.

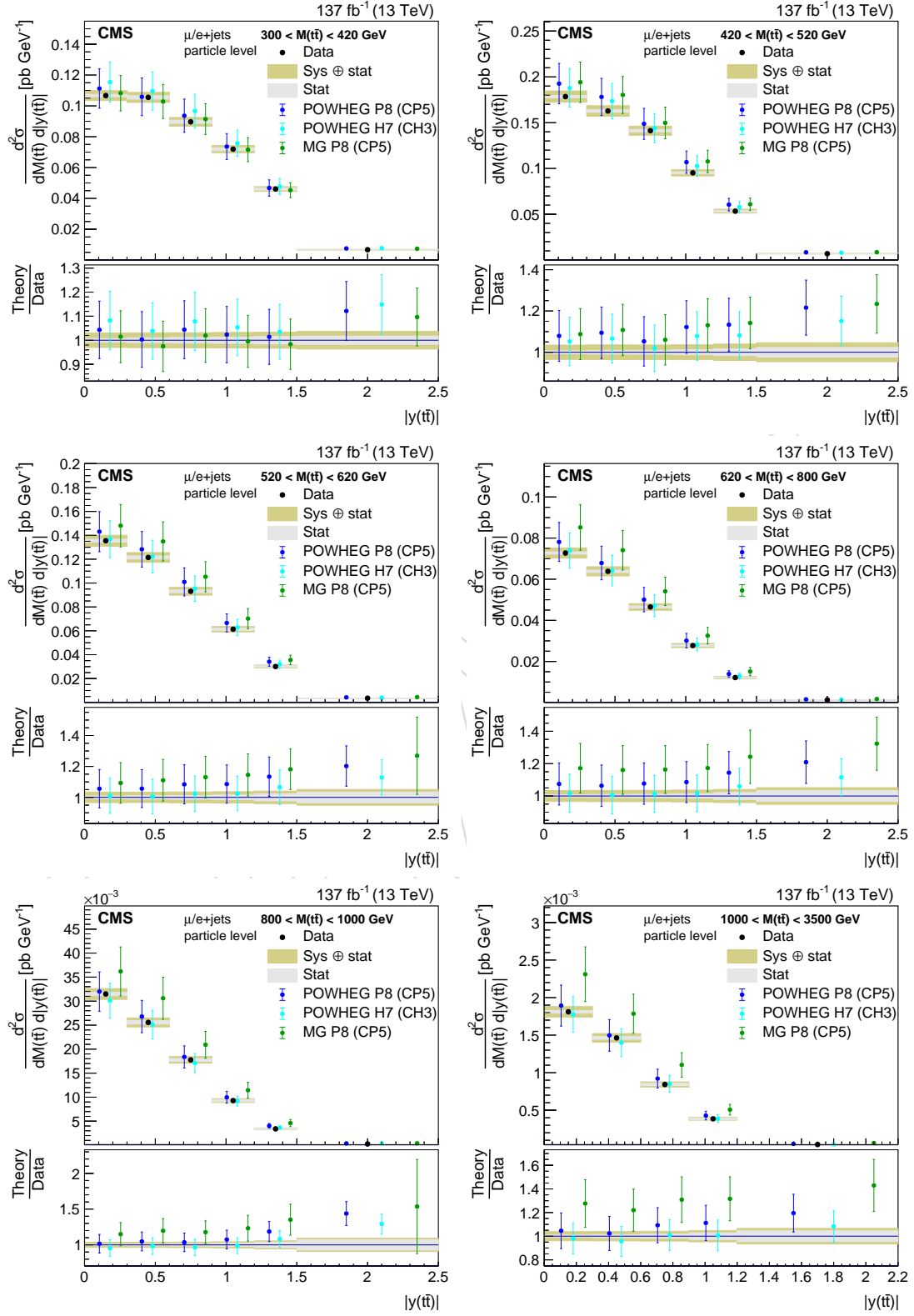
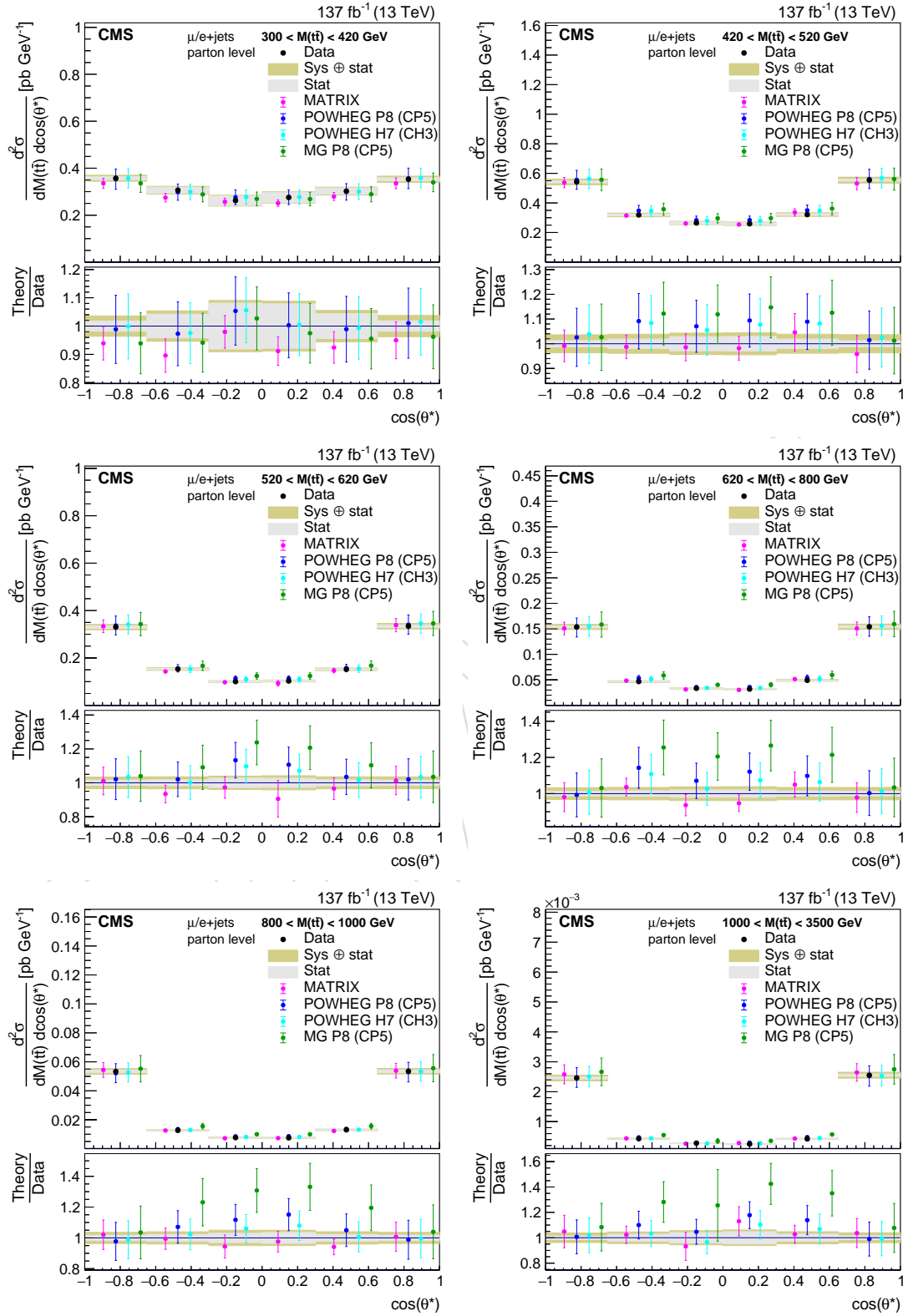


Figure 24: Double differential cross section as function of $M(t\bar{t})$ vs. $|y(t\bar{t})|$.

Figure 25: Double differential cross section as function of $M(t\bar{t})$ vs. $\cos(\theta^*)$.

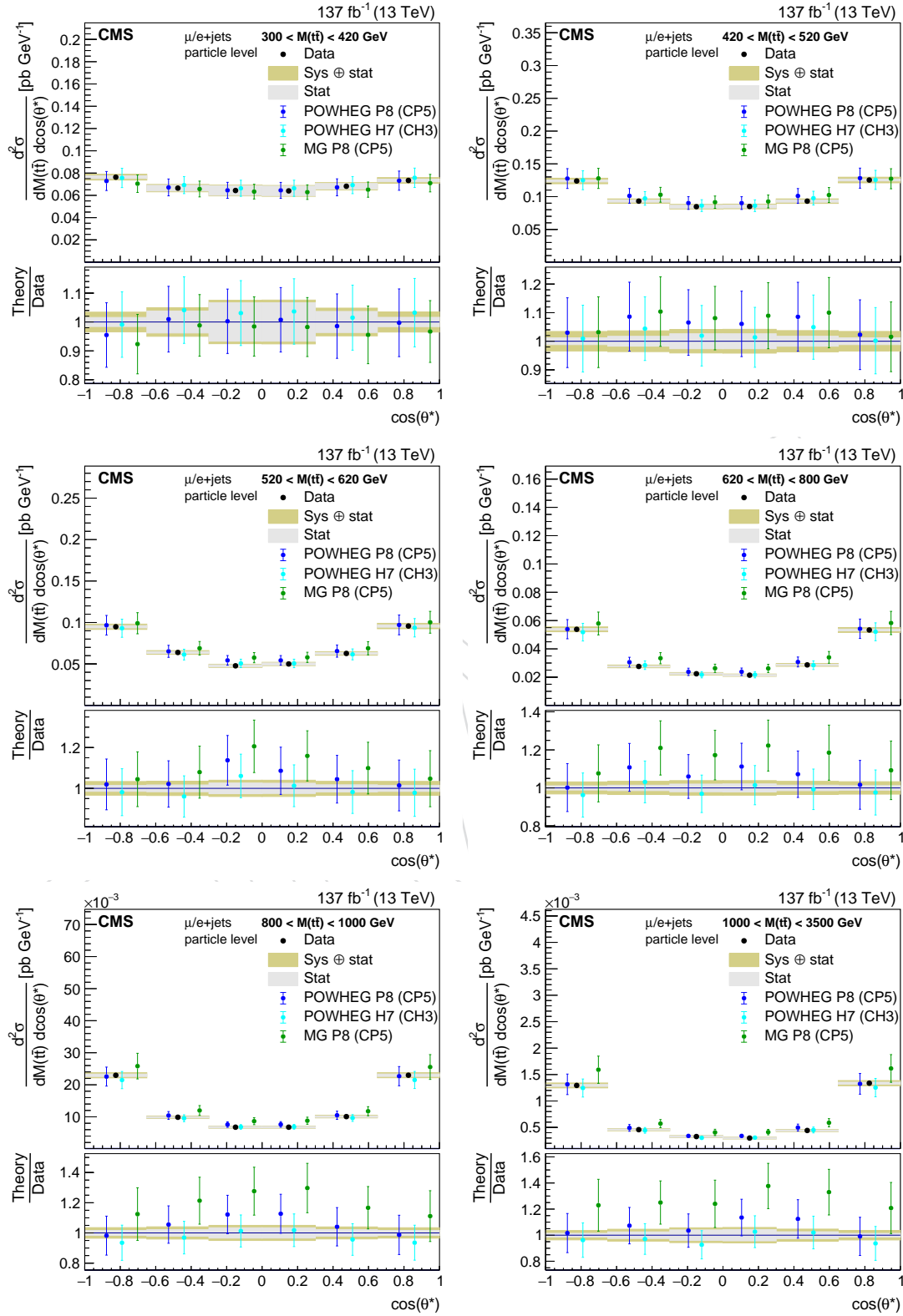
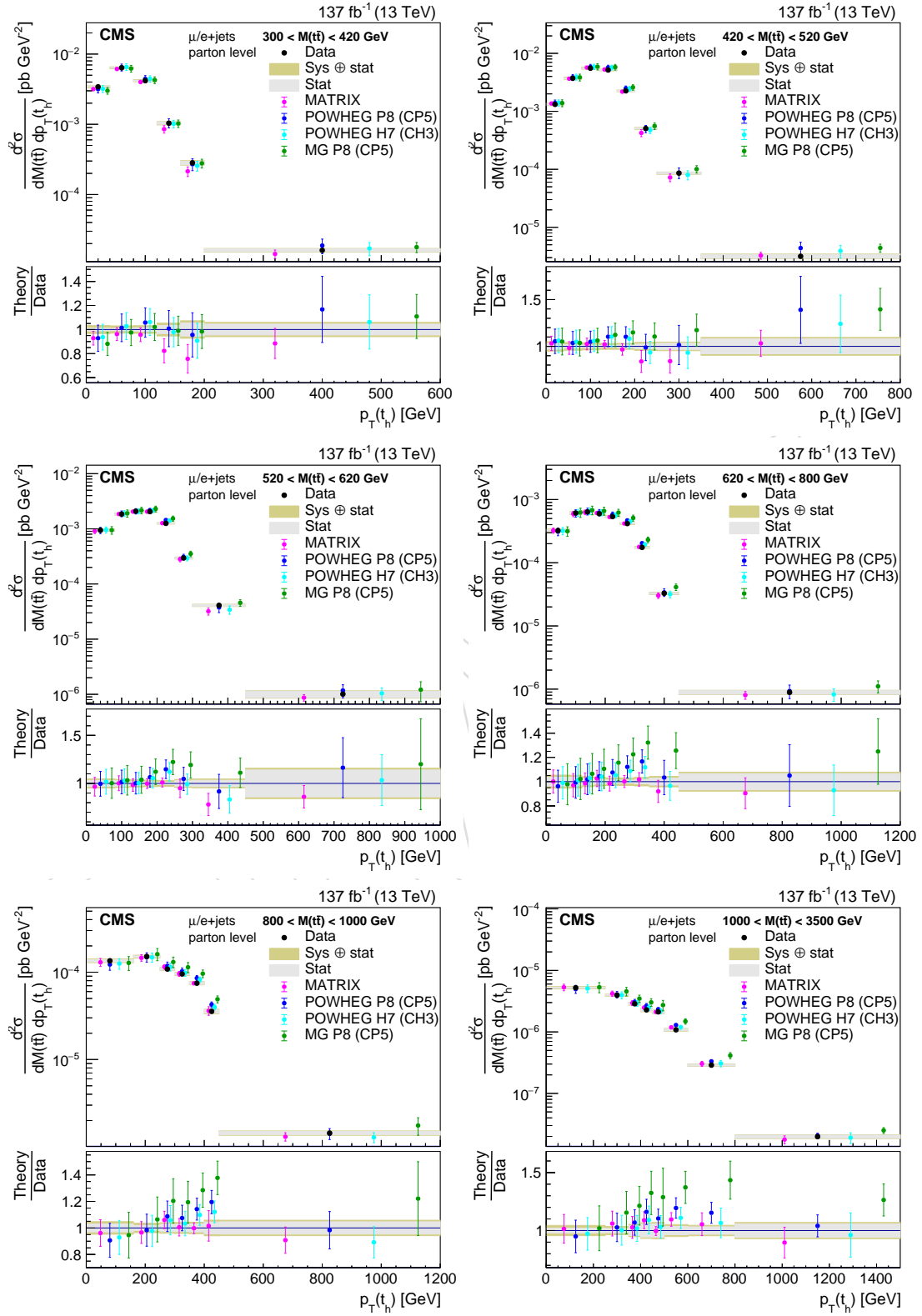


Figure 26: Double differential cross section as function of $M(t\bar{t})$ vs. $\cos(\theta^*)$.

Figure 27: Double differential cross section as function of $M(t\bar{t})$ vs. $p_T(t_h)$.

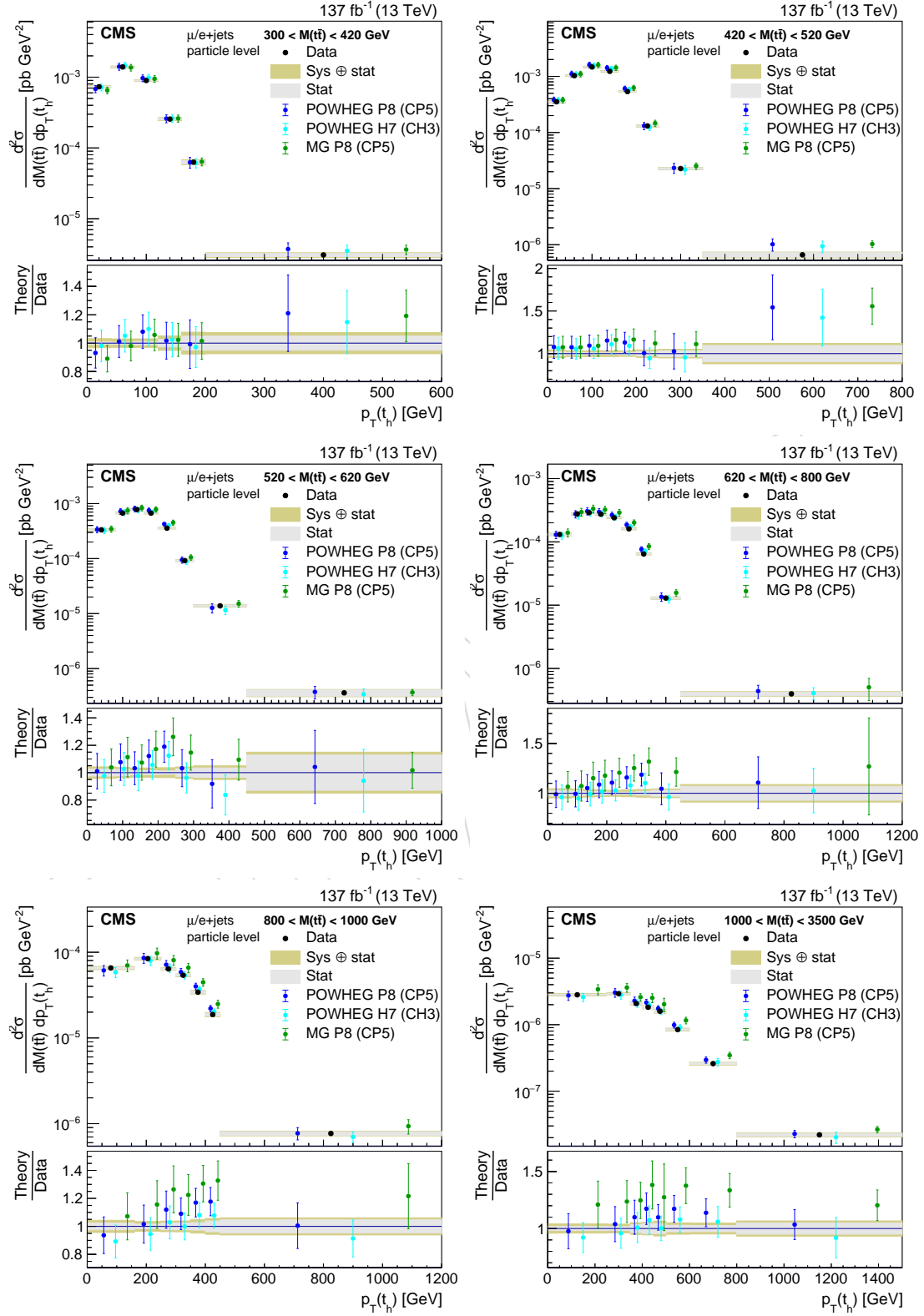
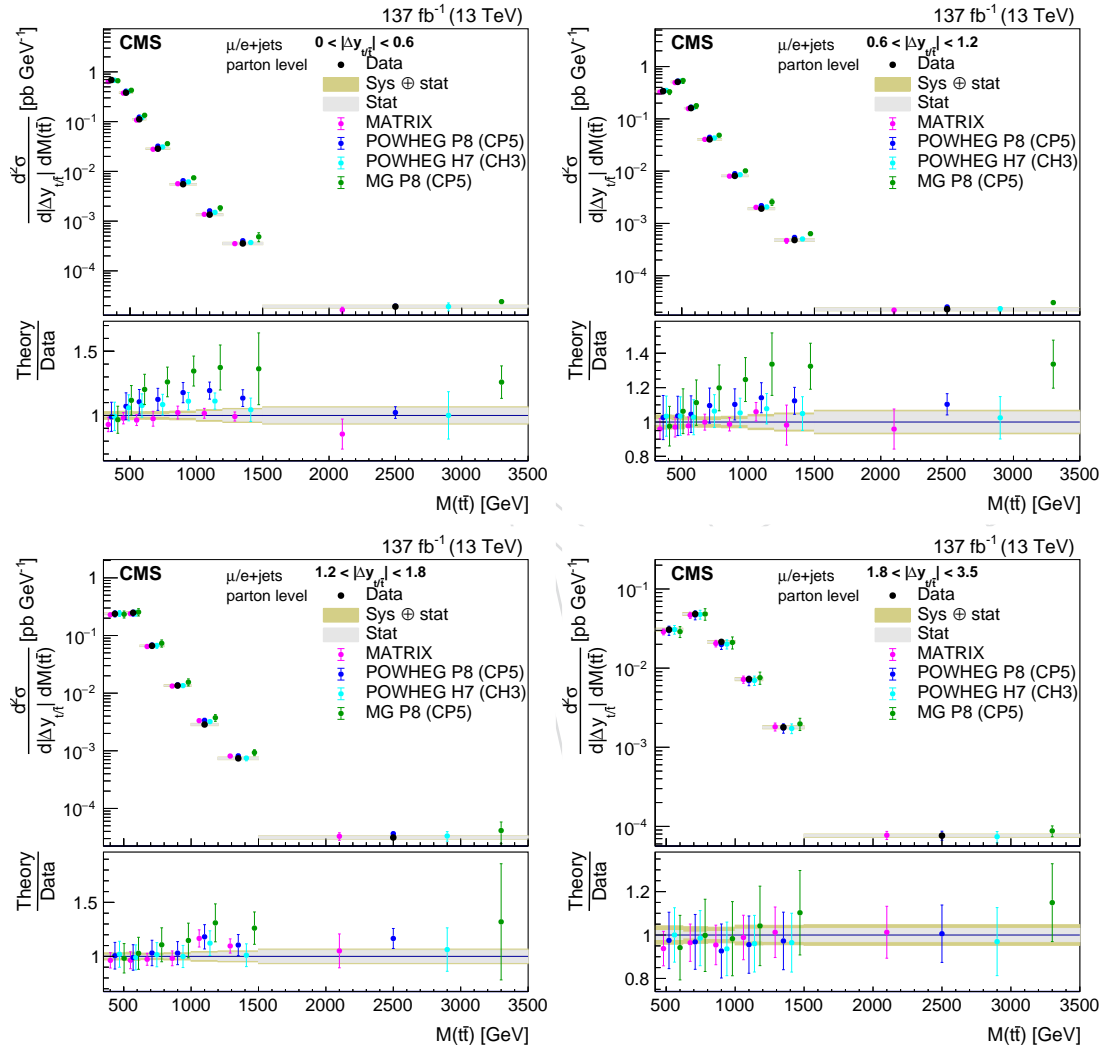


Figure 28: Double differential cross section as function of $M(t\bar{t})$ vs. $p_T(t_h)$.

Figure 29: Double differential cross section as function of $|\Delta y_{t\bar{t}}|$ vs. $M(t\bar{t})$.

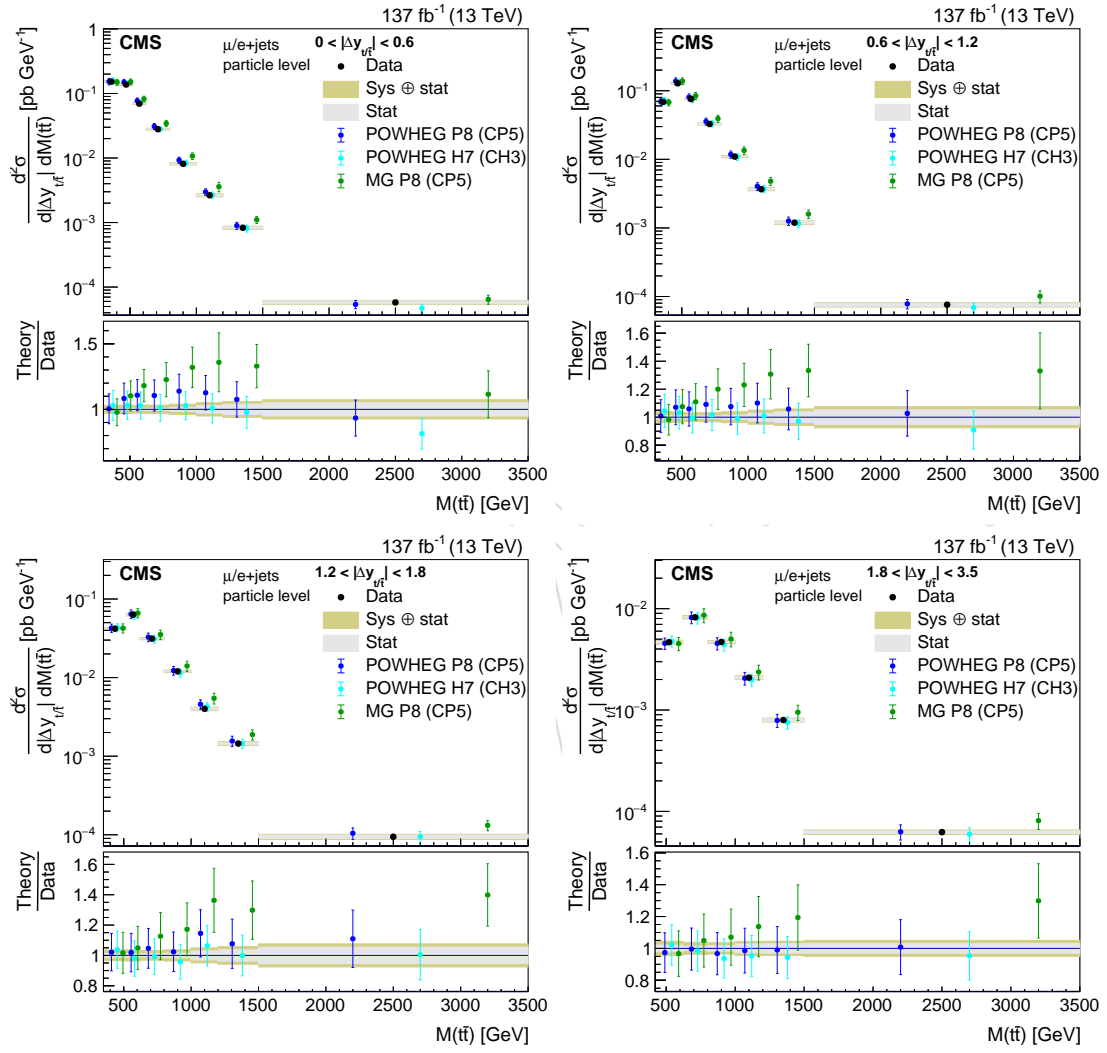
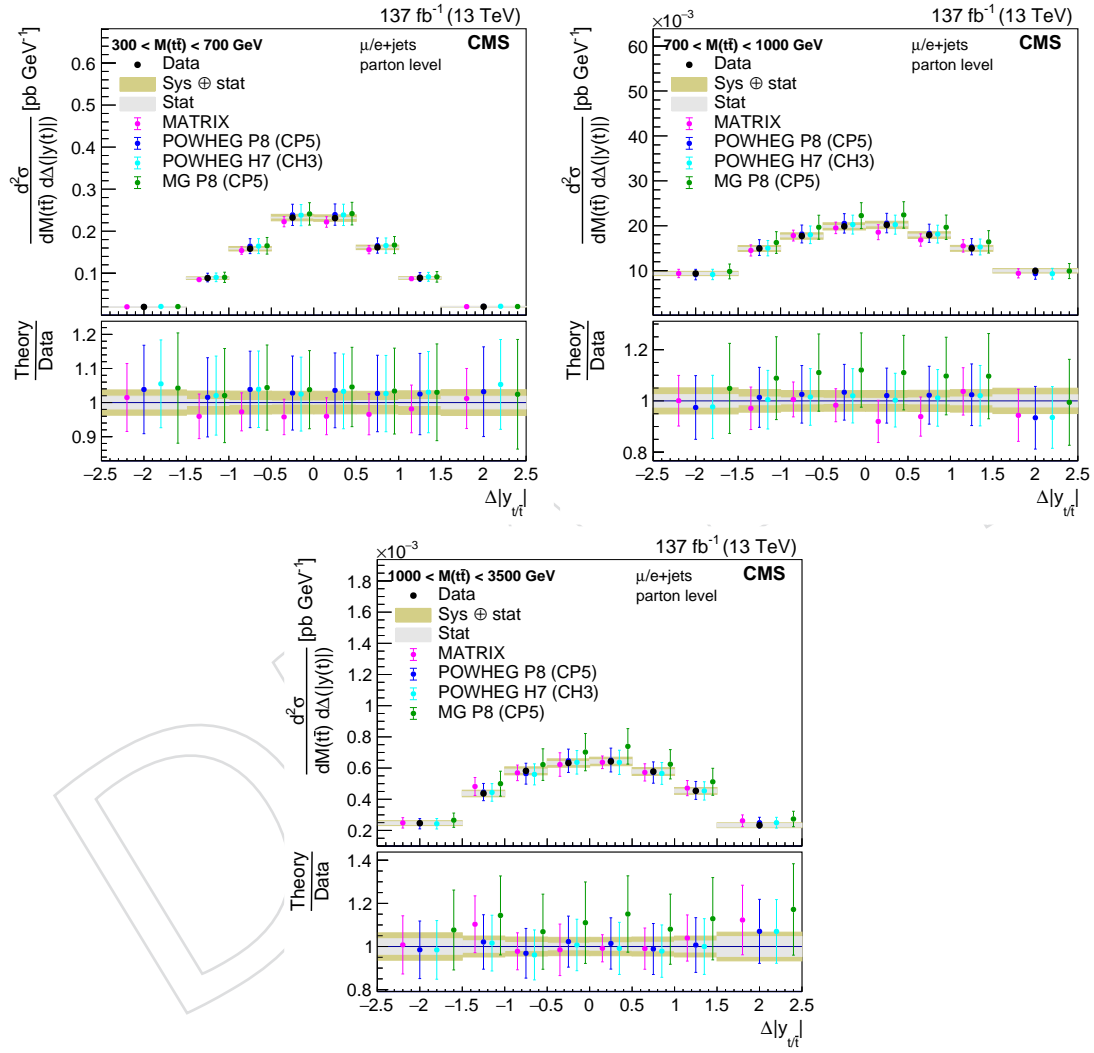


Figure 30: Double differential cross section as function of $|\Delta y_{t/\bar{t}}|$ vs. $M(t\bar{t})$.

Figure 31: Double differential cross section as function of $M(t\bar{t})$ vs. $\Delta|y_{t/\bar{t}}|$.

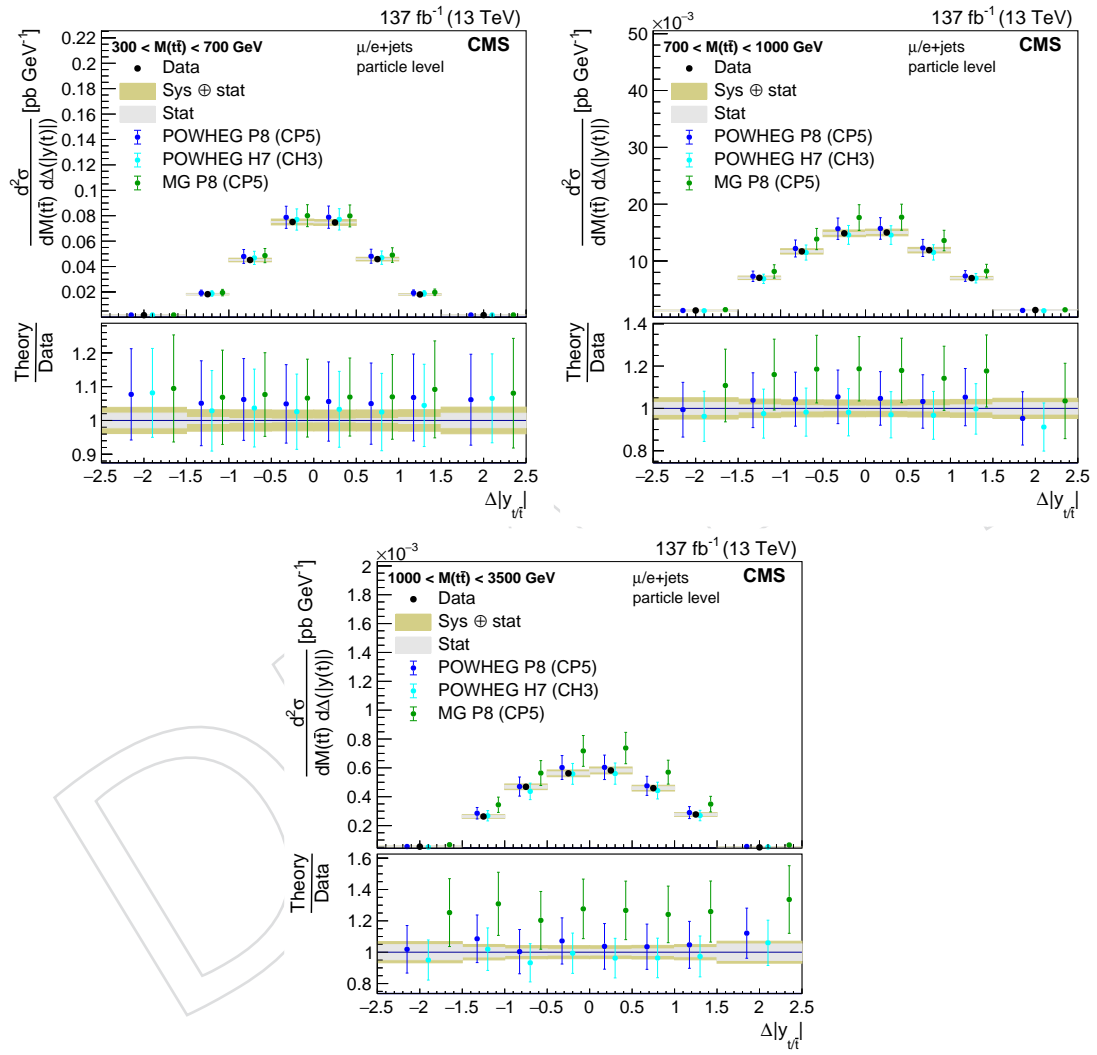


Figure 32: Double differential cross section as function of $M(t\bar{t})$ vs. $\Delta|y_{t/\bar{t}}|$.

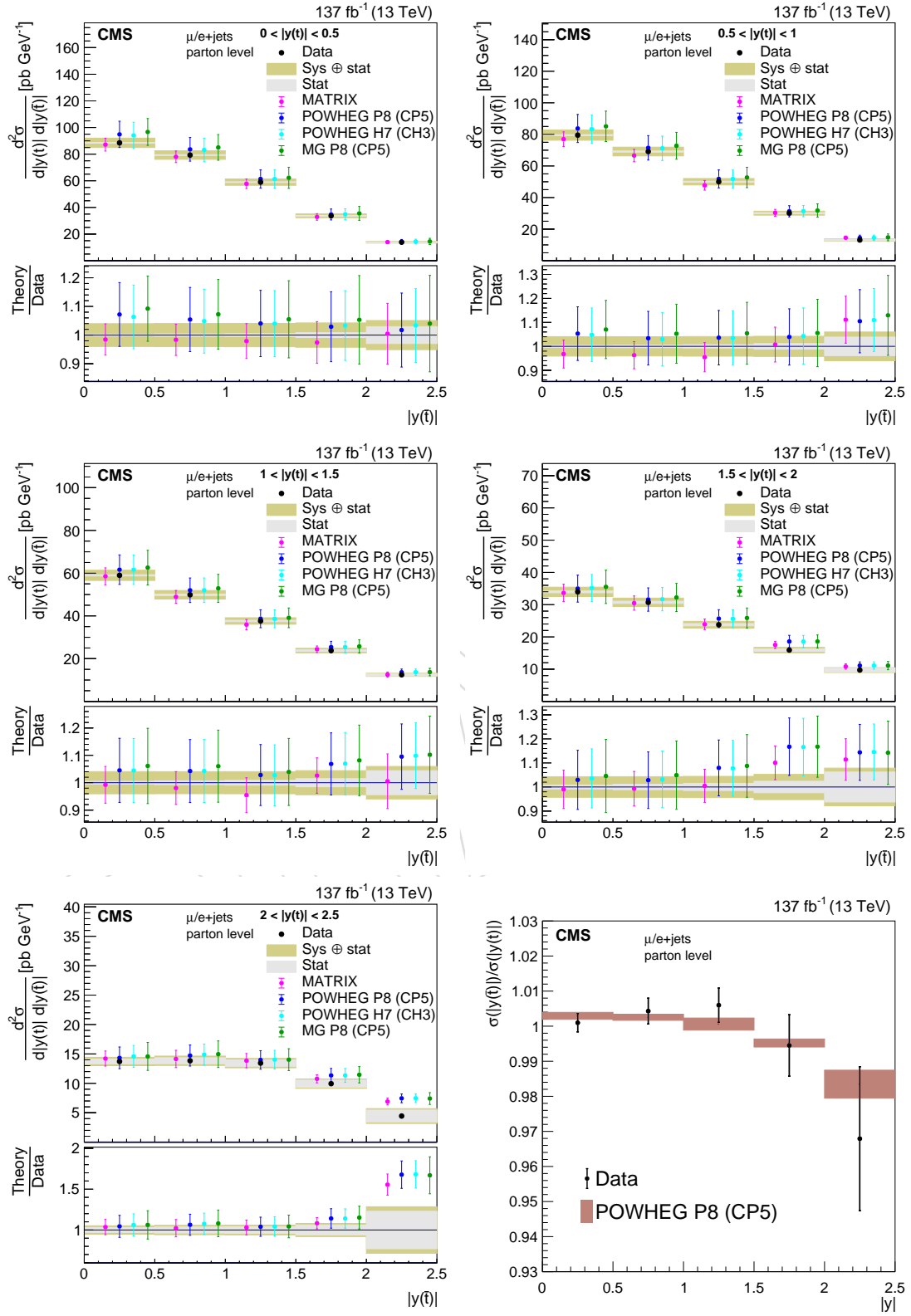


Figure 33: Double differential cross section as function of $|y(t)|$ vs. $|y(\bar{t})|$. Bottom right: ratio of $|y(\bar{t})|/|y(t)|$

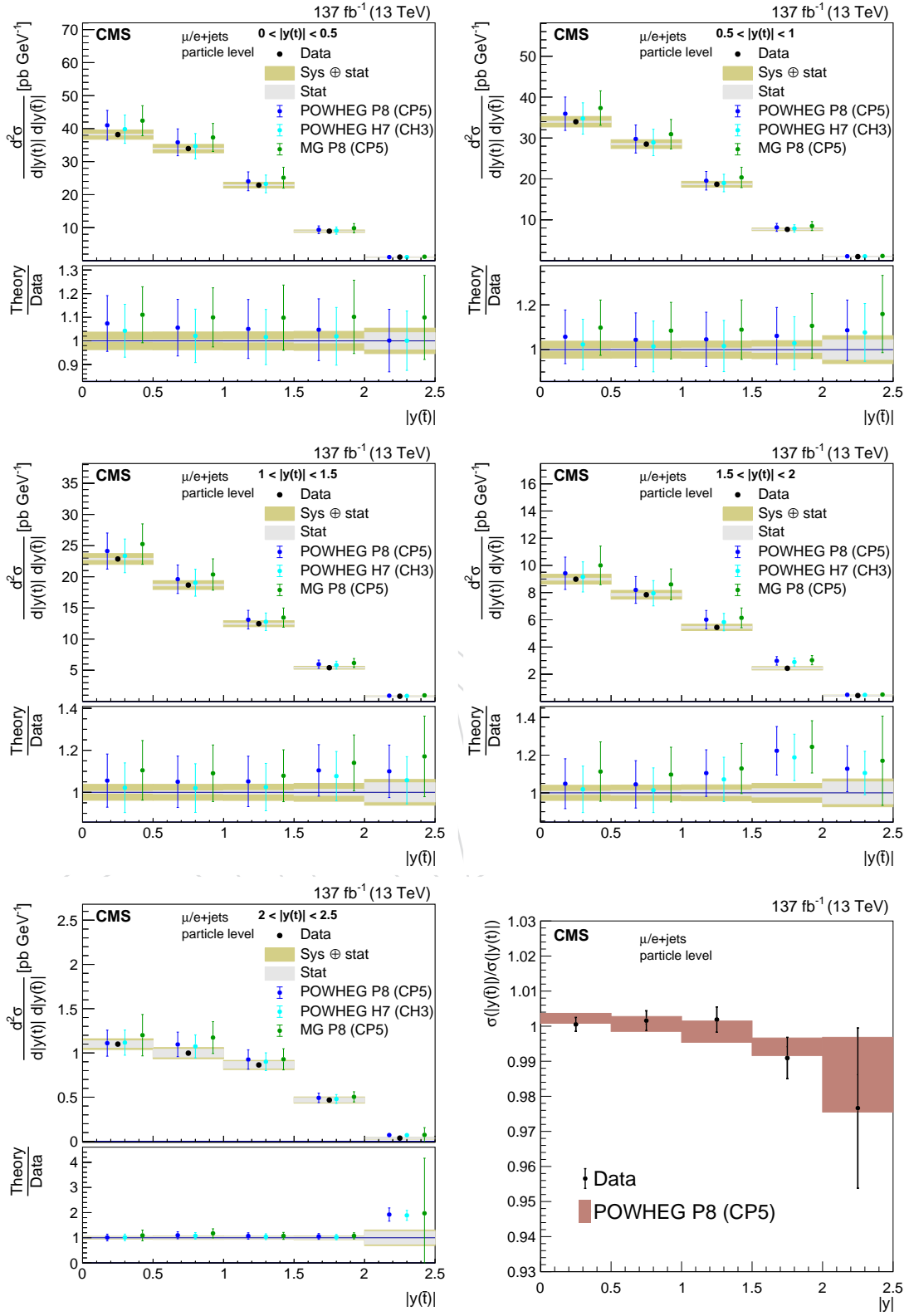


Figure 34: Double differential cross section as function of $|y(t)|$ vs. $|y(\bar{t})|$. Bottom right: ratio of $|y(\bar{t})|/|y(t)|$

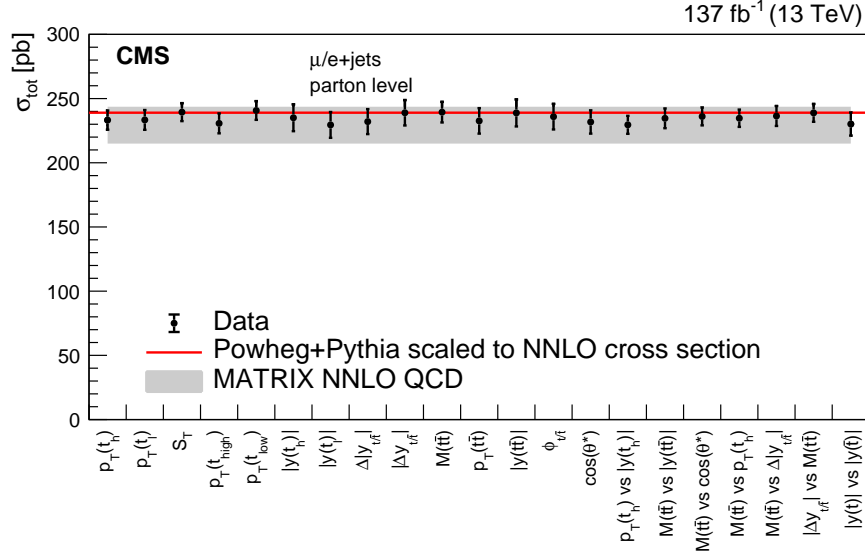


Figure 35: The $t\bar{t}$ production cross sections in the e/μ +jets channel obtained by integrating the differential parton-level measurements. The results are compared to the POWHEG+PYTHIA8 and the MATRIX prediction with its scale uncertainties.

the distribution that can most effectively constrain the systematic uncertainties. In this case, the measurement of $M(t\bar{t})$ vs. $p_T(t_h)$ for which the integrated cross section is

$$\sigma_{e/\mu+jets} = 235 \pm 7.0 \text{ pb.} \quad (7)$$

With a branching fraction of $28.77 \pm 0.32\%$ [41] to e/μ +jets the total $t\bar{t}$ production cross section becomes

$$\sigma_{tot} = 815 \pm 25 \text{ pb.} \quad (8)$$

In Tab. 1 the uncertainties are split into individual sources.

This value is in good agreement with the SM expectation of 799^{+38}_{-50} pb obtained with MATRIX, where the uncertainties include the μ_r and μ_f variations, or the 832^{+40}_{-46} pb obtained with top++2.0 [32] as discussed in Section 2.

By integrating the differential cross sections at particle level the inclusive cross section $\sigma_{particle}$ is obtained. One exception is the cross section as function of H_T . In this distribution events with zero additional jets do not contribute leading to significant lower integrated cross section. As shown in Fig. 36 the integrations of all other distributions result in similar values, where the most precise measurement from $M(t\bar{t})$ vs. $p_T(t_h)$ is

$$\sigma_{particle} = 70.6 \pm 2.0 \text{ pb.} \quad (9)$$

In Tab. 2 the uncertainties are split into individual sources.

In Figs. 37–40 the differential cross section that are only measured at particle level are shown.

Table 1: Systematic uncertainties in the measurement of σ_{tot} .

| Source | Uncertainty [pb] (%) |
|----------------------|----------------------|
| Jet energy | 9.09(1.12) |
| Lepton | 8.91(1.09) |
| b tagging | 6.16(0.76) |
| Mistagging | 3.93(0.48) |
| Pileup | 1.11(0.14) |
| L1 prefire | 0.87(0.11) |
| Background | 5.93(0.73) |
| ISR scale | 3.33(0.41) |
| PDF | 2.76(0.34) |
| NNLO | 2.22(0.27) |
| Scales μ_r/μ_f | 1.31(0.16) |
| h_{damp} | 1.18(0.14) |
| FSR scale | 1.15(0.14) |
| CR model | 0.93(0.11) |
| m_t | 0.71(0.09) |
| Tune | 0.56(0.07) |
| b decay | 0.06(0.01) |
| Luminosity | 14.28(1.75) |
| Sim. stat | 7.08(0.87) |
| Sys | 18.23(2.24) |
| Stat | 0.17(0.02) |
| Luminosity | 13.96(1.73) |

Table 2: Systematic uncertainties in the measurement of σ_{particle} .

| Source | Uncertainty [pb] (%) |
|----------------------|----------------------|
| Lepton | 0.81(1.15) |
| Jet energy | 0.70(0.99) |
| b tagging | 0.59(0.84) |
| Mistagging | 0.27(0.38) |
| L1 prefire | 0.05(0.08) |
| Background | 0.43(0.61) |
| Pileup | 0.12(0.17) |
| FSR scale | 0.24(0.34) |
| PDF | 0.21(0.30) |
| Scales μ_r/μ_f | 0.13(0.19) |
| CR model | 0.10(0.15) |
| b decay | 0.08(0.11) |
| h_{damp} | 0.05(0.08) |
| Tune | 0.04(0.06) |
| m_t | 0.04(0.06) |
| NNLO | 0.04(0.05) |
| ISR scale | 0.01(0.02) |
| Sim. stat | 0.81(1.15) |
| Sys | 1.6(2.3) |
| Stat | 0.05(0.07) |
| Luminosity | 1.23(1.75) |

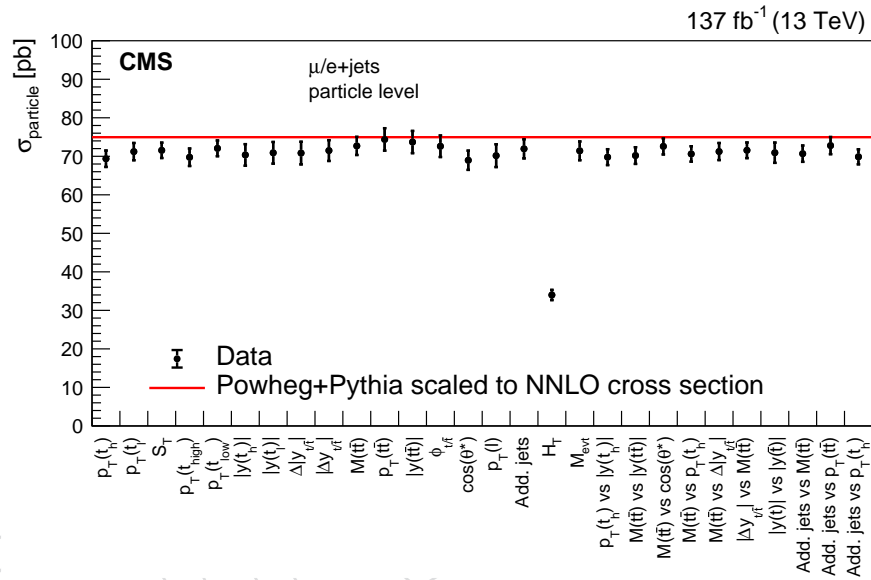


Figure 36: The $t\bar{t}$ production cross sections σ_{particle} obtained by integrating the differential particle-level measurements. The results are compared to the POWHEG+PYTHIA8 predictions.

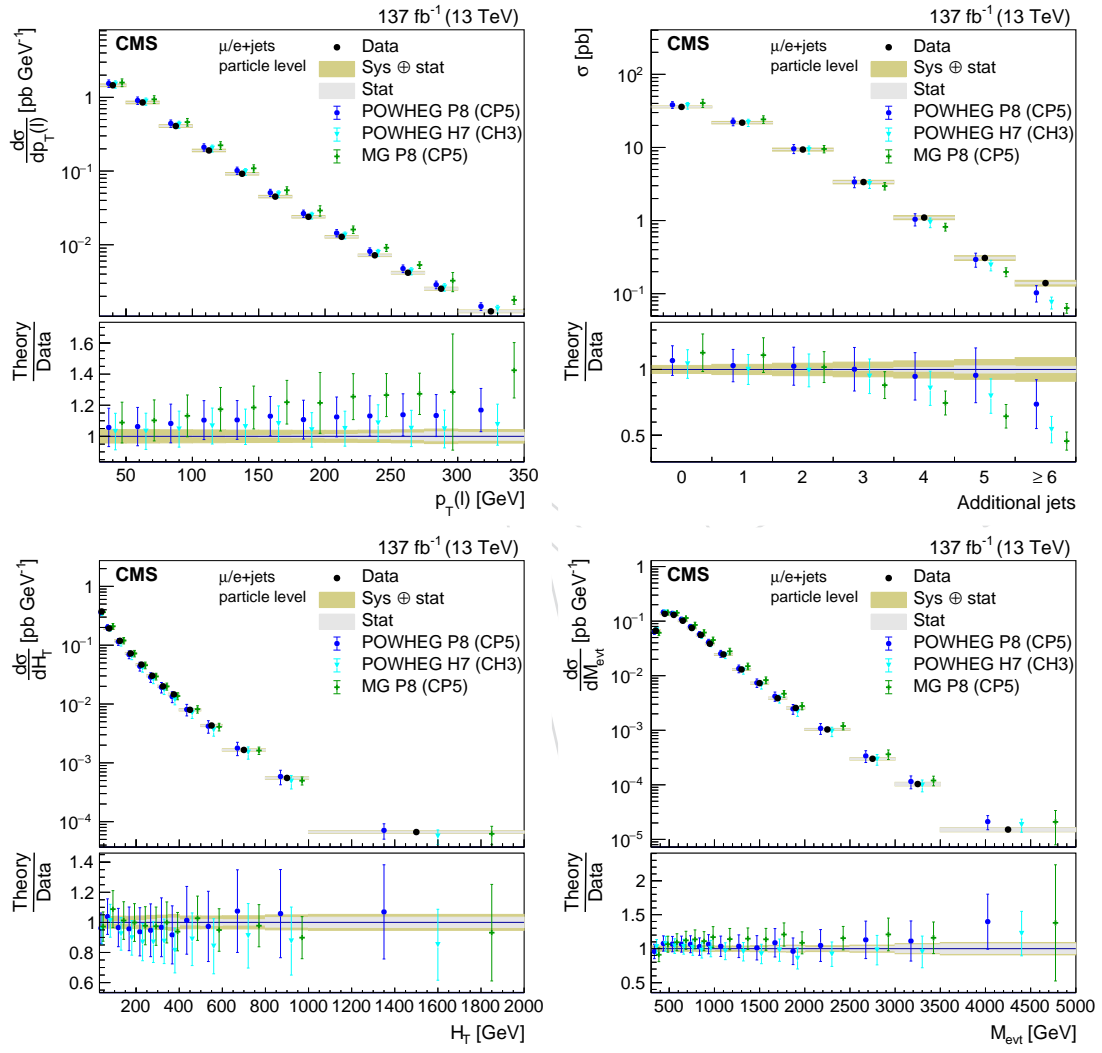
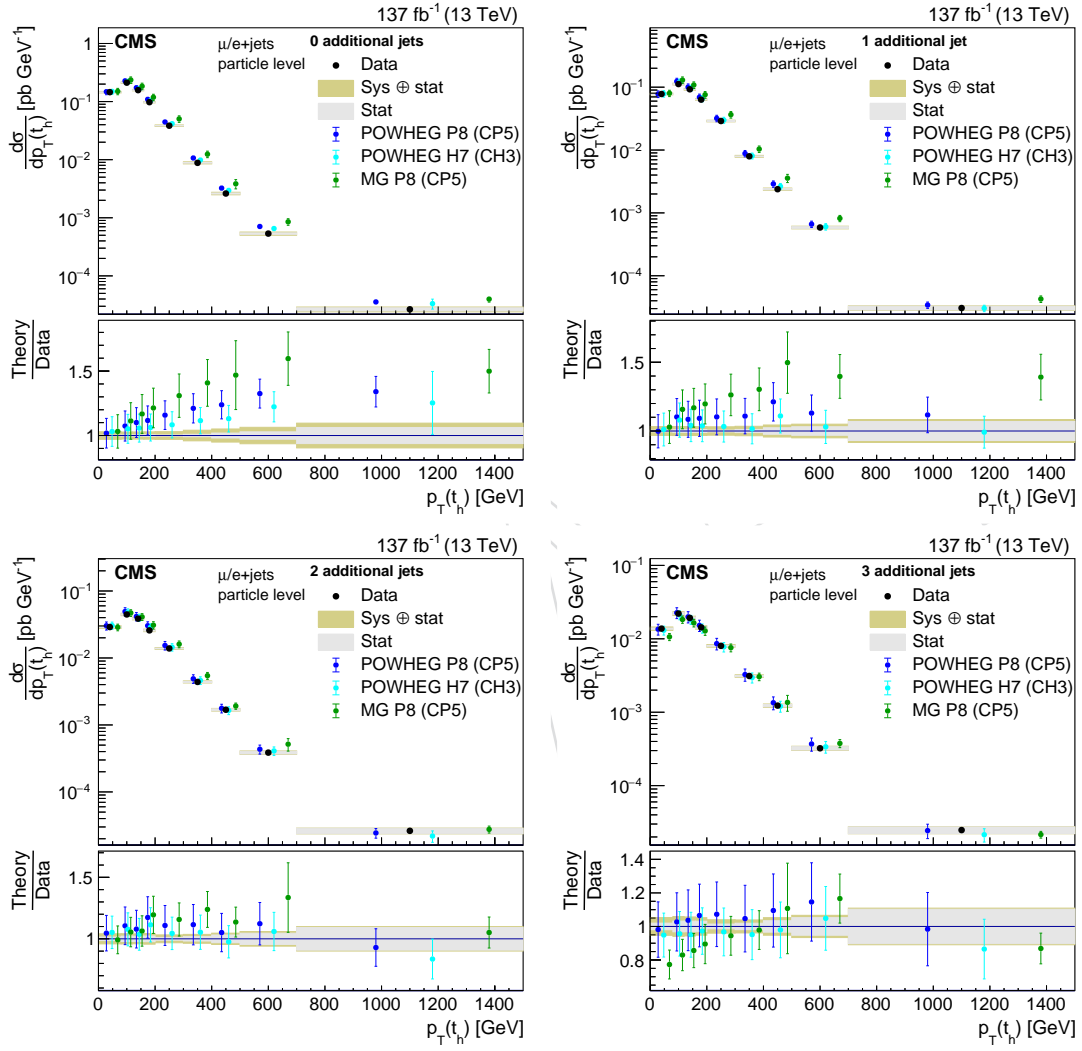


Figure 37: Differential cross sections as functions of $p_T(\ell)$, jet multiplicity, H_T , and M_{evt} .

Figure 38: Differential cross section as function of $p_T(t_h)$ in bins of jet multiplicity.

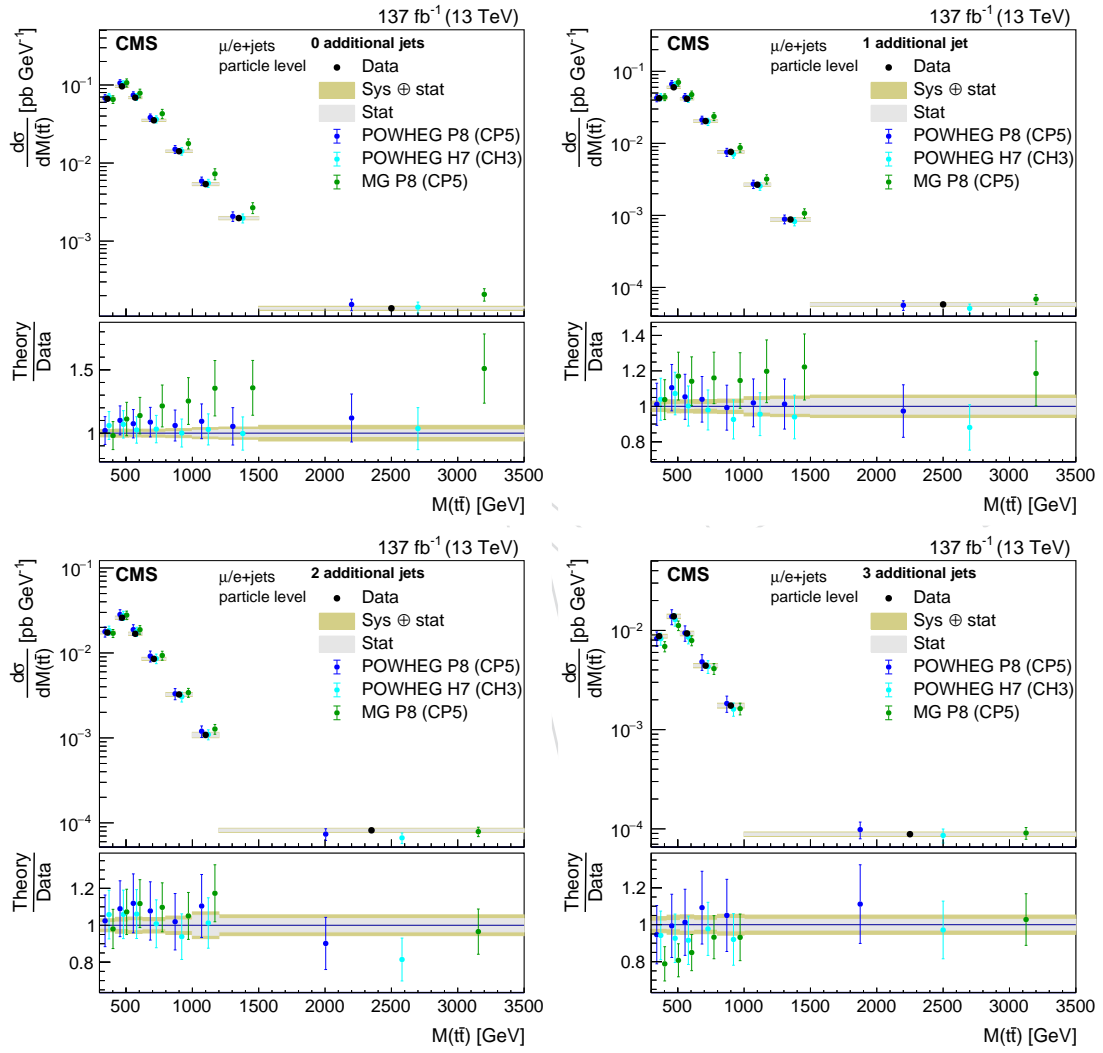
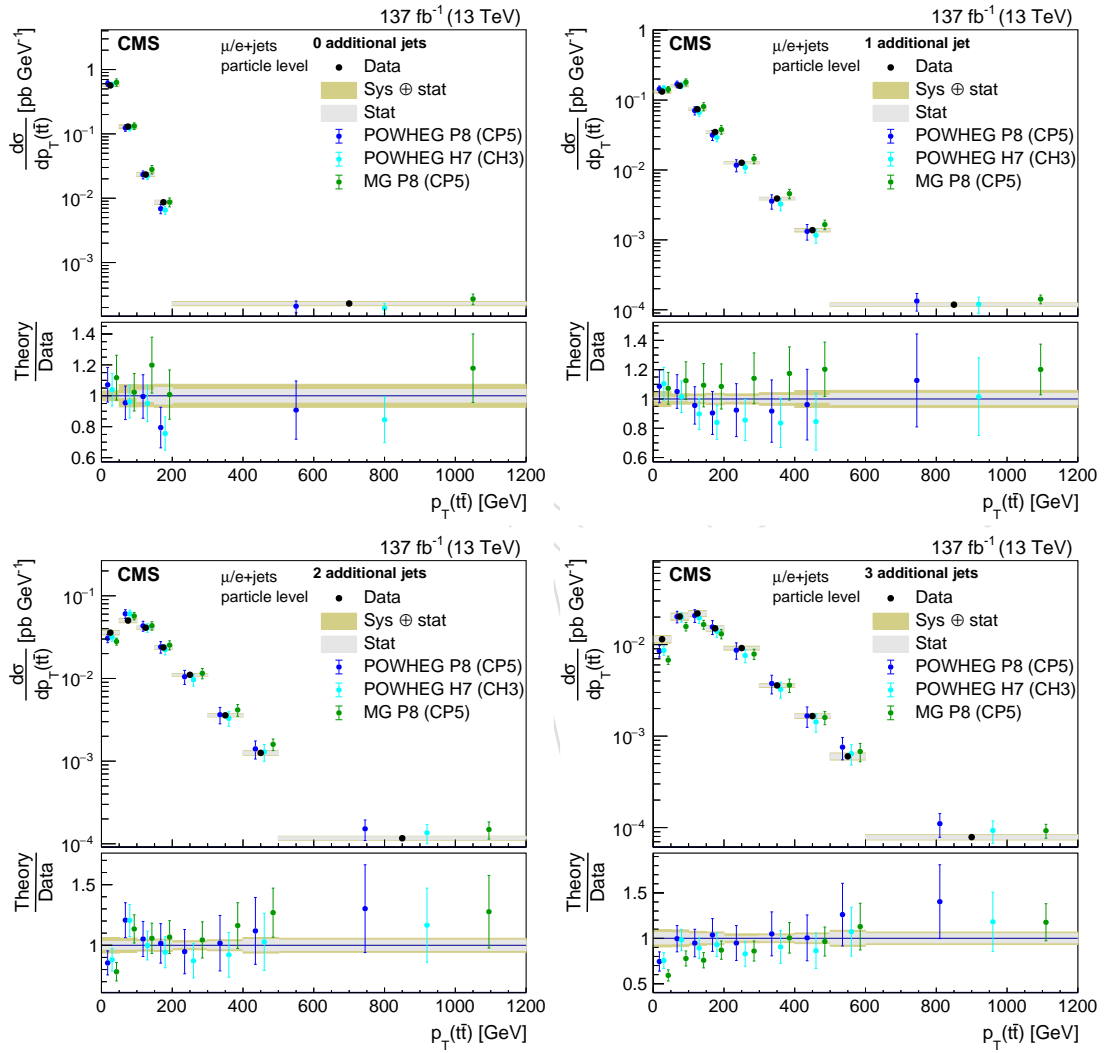


Figure 39: Differential cross section as function of $M(t\bar{t})$ in bins of jet multiplicity.

Figure 40: Differential cross section as function of $p_T(t\bar{t})$ in bins of jet multiplicity.

15 Summary

A measurement of the differential and double differential $t\bar{t}$ production cross sections was presented as functions of many kinematic properties of the top quarks and the $t\bar{t}$ system at parton and particle levels. In addition, the number of additional jets and kinematic variables in bins of jet multiplicities have been measured at particle level. The data correspond to an integrated luminosity of 137 fb^{-1} recorded by the CMS experiment. The $t\bar{t}$ cross sections are measured in the e/μ +jets channels. For the first time the cross section of the full spectra are obtained using a combination of resolved and boosted $t\bar{t}$ topologies. The combination of multiple reconstruction categories allow for constraints of systematic uncertainties and result in a significantly improved precision with respect to previous measurements. Uncertainties in the jet energy scale, luminosity, and $t\bar{t}$ modelling are the dominant sources.

In general, most differential distributions are found to be compatible with the SM predictions of POWHEG+PYTHIA8, POWHEG+HERWIG, and MG5_aMC@NLO+PYTHIA8. However, some tension is observed at high rapidities of the top quarks and the $t\bar{t}$ system. The simulation by POWHEG+HERWIG and MG5_aMC@NLO+PYTHIA8 have problems to describe the jet multiplicities and related observables like H_T . The measured inclusive $t\bar{t}$ production cross section is

$$\sigma_{\text{tot}} = 815 \pm 25 \text{ pb.} \quad (10)$$

and in good agreement with the SM expectation.

Acknowledgments

References

- [1] CMS Collaboration, “Measurement of differential top-quark pair production cross sections in pp collisions at $\sqrt{s} = 7 \text{ TeV}$ ”, *Eur. Phys. J. C* **73** (2013) 2339, doi:10.1140/epjc/s10052-013-2339-4, arXiv:1211.2220.
- [2] ATLAS Collaboration, “Differential top-antitop cross-section measurements as a function of observables constructed from final-state particles using pp collisions at $\sqrt{s} = 7 \text{ TeV}$ in the ATLAS detector”, *JHEP* **06** (2015) 100, doi:10.1007/JHEP06(2015)100, arXiv:1502.05923.
- [3] CMS Collaboration, “Measurement of the differential cross section for top quark pair production in pp collisions at $\sqrt{s} = 8 \text{ TeV}$ ”, *Eur. Phys. J. C* **75** (2015) 542, doi:10.1140/epjc/s10052-015-3709-x, arXiv:1505.04480.
- [4] ATLAS Collaboration, “Measurements of top-quark pair differential cross-sections in the lepton+jets channel in pp collisions at $\sqrt{s} = 8 \text{ TeV}$ using the ATLAS detector”, *Eur. Phys. J. C* **76** (2016) 538, doi:10.1140/epjc/s10052-016-4366-4, arXiv:1511.04716.
- [5] ATLAS Collaboration, “Measurement of the differential cross-section of highly boosted top quarks as a function of their transverse momentum in $\sqrt{s} = 8 \text{ TeV}$ proton-proton collisions using the ATLAS detector”, *Phys. Rev. D* **93** (2016) 032009, doi:10.1103/PhysRevD.93.032009, arXiv:1510.03818.
- [6] CMS Collaboration, “Measurement of the $t\bar{t}$ production cross section in the all-jets final state in pp collisions at $\sqrt{s} = 8 \text{ TeV}$ ”, *Eur. Phys. J. C* **76** (2016) 128, doi:10.1140/epjc/s10052-016-3956-5, arXiv:1509.06076.

- [7] CMS Collaboration, “Measurement of the integrated and differential $t\bar{t}$ production cross sections for high- p_T top quarks in pp collisions at $\sqrt{s} = 8$ TeV”, *Phys. Rev. D* **94** (2016) 072002, doi:10.1103/PhysRevD.94.072002, arXiv:1605.00116.
- [8] ATLAS Collaboration, “Measurement of top quark pair differential cross-sections in the dilepton channel in pp collisions at $\sqrt{s} = 7$ and 8 TeV with ATLAS”, *Phys. Rev. D* **94** (2016) 092003, doi:10.1103/PhysRevD.94.092003, arXiv:1607.07281.
- [9] CMS Collaboration, “Measurement of double-differential cross sections for top quark pair production in pp collisions at $\sqrt{s} = 8$ TeV and impact on parton distribution functions”, *Eur. Phys. J. C* **77** (2017) 459, doi:10.1140/epjc/s10052-017-4984-5, arXiv:1703.01630.
- [10] ATLAS Collaboration, “Measurement of jet activity produced in top-quark events with an electron, a muon and two b-tagged jets in the final state in pp collisions at $\sqrt{s} = 13$ TeV with the ATLAS detector”, *Eur. Phys. J. C* **77** (2017) 220, doi:10.1140/epjc/s10052-017-4766-0, arXiv:1610.09978.
- [11] ATLAS Collaboration, “Measurements of top-quark pair differential cross-sections in the $e\mu$ channel in pp collisions at $\sqrt{s} = 13$ TeV using the ATLAS detector”, *Eur. Phys. J. C* **77** (2017) 292, doi:10.1140/epjc/s10052-017-4821-x, arXiv:1612.05220.
- [12] CMS Collaboration, “Measurement of normalized differential $t\bar{t}$ cross sections in the dilepton channel from pp collisions at $\sqrt{s} = 13$ TeV.”, (2017). arXiv:1708.07638. Submitted to *JHEP*.
- [13] CMS Collaboration, “Measurement of differential cross sections for top quark pair production using the lepton+jets final state in proton-proton collisions at 13 TeV”, *Phys. Rev. D* **95** (2017) 092001, doi:10.1103/PhysRevD.95.092001, arXiv:1610.04191.
- [14] CMS Collaboration, “Measurement of differential cross sections for the production of top quark pairs and of additional jets in lepton+jets events from pp collisions at 13 TeV”, *Phys. Rev. D* **97** (2018) 112003, doi:10.1103/PhysRevD.97.112003, arXiv:1803.08856.
- [15] ATLAS Collaboration, “Measurements of $t\bar{t}$ differential cross-sections of highly boosted top quarks decaying to all-hadronic final states in pp collisions at $\sqrt{s} = 13$ TeV using the ATLAS detector”, *Phys. Rev. D* **98** (2018) 012003, doi:10.1103/PhysRevD.98.012003, arXiv:1801.02052.
- [16] ATLAS Collaboration, “Measurements of top-quark pair differential and double-differential cross-sections in the ℓ +jets channel with pp collisions at $\sqrt{s} = 13$ TeV using the ATLAS detector”, *Eur. Phys. J. C* **79** (2019) 1028, doi:10.1140/epjc/s10052-019-7525-6, arXiv:1908.07305.
- [17] ATLAS Collaboration, “Measurement of the $t\bar{t}$ production cross-section and lepton differential distributions in $e\mu$ dilepton events from pp collisions at $\sqrt{s} = 13$ TeV with the ATLAS detector”, *Submitted to Eur. Phys. J. C* (2019) arXiv:1910.08819.
- [18] P. Nason, “A new method for combining NLO QCD with shower Monte Carlo algorithms”, *JHEP* **11** (2004) 040, doi:10.1088/1126-6708/2004/11/040, arXiv:hep-ph/0409146.

- [19] S. Frixione, P. Nason, and C. Oleari, “Matching NLO QCD computations with parton shower simulations: the POWHEG method”, *JHEP* **11** (2007) 070, doi:10.1088/1126-6708/2007/11/070, arXiv:0709.2092.
- [20] S. Alioli, P. Nason, C. Oleari, and E. Re, “A general framework for implementing NLO calculations in shower Monte Carlo programs: the POWHEG BOX”, *JHEP* **06** (2010) 043, doi:10.1007/JHEP06(2010)043, arXiv:1002.2581.
- [21] J. M. Campbell, R. K. Ellis, P. Nason, and E. Re, “Top-pair production and decay at NLO matched with parton showers”, *JHEP* **04** (2015) 114, doi:10.1007/JHEP04(2015)114, arXiv:1412.1828.
- [22] T. Sjöstrand, S. Mrenna, and P. Skands, “PYTHIA 6.4 physics and manual”, *JHEP* **05** (2006) 026, doi:10.1088/1126-6708/2006/05/026, arXiv:hep-ph/0603175.
- [23] T. Sjöstrand, S. Mrenna, and P. Skands, “A brief introduction to PYTHIA 8.1”, *Comput. Phys. Commun.* **178** (2008) 852, doi:10.1016/j.cpc.2008.01.036, arXiv:0710.3820.
- [24] P. Skands, S. Carrazza, and J. Rojo, “Tuning PYTHIA 8.1: the Monash 2013 tune”, *Eur. Phys. J. C* **74** (2014) 3024, doi:10.1140/epjc/s10052-014-3024-y, arXiv:1404.5630.
- [25] CMS Collaboration, “Investigations of the impact of the parton shower tuning in PYTHIA 8 in the modelling of $t\bar{t}$ at $\sqrt{s} = 8$ and 13 TeV”, CMS Physics Analysis Summary CMS-PAS-TOP-16-021, 2016.
- [26] NNPDF Collaboration, “Parton distributions for the LHC Run II”, *JHEP* **04** (2015) 040, doi:10.1007/JHEP04(2015)040, arXiv:1410.8849.
- [27] NNPDF Collaboration, “Parton distributions from high-precision collider data”, *Eur. Phys. J. C* **77** (2017) 663, doi:10.1140/epjc/s10052-017-5199-5, arXiv:1706.00428.
- [28] GEANT4 Collaboration, “GEANT4—a simulation toolkit”, *Nucl. Instrum. Meth. A* **506** (2003) 250, doi:10.1016/S0168-9002(03)01368-8.
- [29] M. Bähr et al., “HERWIG++ physics and manual”, *Eur. Phys. J. C* **58** (2008) 639, doi:10.1140/epjc/s10052-008-0798-9, arXiv:0803.0883.
- [30] J. Alwall et al., “The automated computation of tree-level and next-to-leading order differential cross sections, and their matching to parton shower simulations”, *JHEP* **07** (2014) 079, doi:10.1007/JHEP07(2014)079, arXiv:1405.0301.
- [31] R. Frederix and S. Frixione, “Merging meets matching in MC@NLO”, *JHEP* **12** (2012) 061, doi:10.1007/JHEP12(2012)061, arXiv:1209.6215.
- [32] M. Czakon and A. Mitov, “Top++: A program for the calculation of the top-pair cross-section at hadron colliders”, *Comput. Phys. Commun.* **185** (2014) 2930, doi:10.1016/j.cpc.2014.06.021, arXiv:1112.5675.
- [33] M. Grazzini, S. Kallweit, and M. Wiesemann, “Fully differential NNLO computations with MATRIX”, *Eur. Phys. J. C* **78** (2017) 537, doi:10.1140/epjc/s10052-018-5771-7, arXiv:1711.06631.

- [34] E. Re, “Single-top Wt-channel production matched with parton showers using the POWHEG method”, *Eur. Phys. J. C* **71** (2011) 1547, doi:10.1140/epjc/s10052-011-1547-z, arXiv:1009.2450.
- [35] Y. Li and F. Petriello, “Combining QCD and electroweak corrections to dilepton production in FEWZ”, *Phys. Rev. D* **86** (2012) 094034, doi:10.1103/PhysRevD.86.094034, arXiv:1208.5967.
- [36] P. Kant et al., “HatHor for single top-quark production: Updated predictions and uncertainty estimates for single top-quark production in hadronic collisions”, *Comput. Phys. Commun.* **191** (2015) 74, doi:10.1016/j.cpc.2015.02.001, arXiv:1406.4403.
- [37] N. Kidonakis, “NNLL threshold resummation for top-pair and single-top production”, *Phys. Part. Nucl.* **45** (2014) 714, doi:10.1134/S1063779614040091, arXiv:1210.7813.
- [38] CMS Collaboration, “Object definitions for top quark analyses at the particle level”, CMS Note CERN-CMS-NOTE-2017-004, 2017.
- [39] M. Cacciari, G. P. Salam, and G. Soyez, “The anti- k_t jet clustering algorithm”, *JHEP* **04** (2008) 063, doi:10.1088/1126-6708/2008/04/063, arXiv:0802.1189.
- [40] M. Cacciari, G. P. Salam, and G. Soyez, “FastJet user manual”, *Eur. Phys. J. C* **72** (2012) 1896, doi:10.1140/epjc/s10052-012-1896-2, arXiv:1111.6097.
- [41] Particle Data Group, C. Patrignani et al., “Review of particle physics”, *Chin. Phys. C* **40** (2016) 100001, doi:10.1088/1674-1137/40/10/100001.
- [42] CMS Collaboration, “The CMS experiment at the CERN LHC”, *JINST* **3** (2008) S08004, doi:10.1088/1748-0221/3/08/S08004.
- [43] CMS Collaboration, “Particle-flow reconstruction and global event description with the CMS detector”, *JINST* **12** (2017) P10003, doi:10.1088/1748-0221/12/10/P10003, arXiv:1706.04965.
- [44] CMS Collaboration, “Measurements of inclusive W and Z cross sections in pp collisions at $\sqrt{s} = 7$ TeV”, *JHEP* **01** (2011) 080, doi:10.1007/JHEP01(2011)080, arXiv:1012.2466.
- [45] CMS Collaboration, “Performance of CMS muon reconstruction in pp collision events at $\sqrt{s} = 7$ TeV”, *JINST* **7** (2012) P10002, doi:10.1088/1748-0221/7/10/P10002, arXiv:1206.4071.
- [46] CMS Collaboration, “Performance of electron reconstruction and selection with the CMS detector in proton-proton collisions at $\sqrt{s} = 8$ TeV”, *JINST* **10** (2015) P06005, doi:10.1088/1748-0221/10/06/P06005, arXiv:1502.02701.
- [47] CMS Collaboration, “Jet energy scale and resolution in the CMS experiment in pp collisions at 8 TeV”, *JINST* **12** (2017) P02014, doi:10.1088/1748-0221/12/02/P02014, arXiv:1607.03663.
- [48] CMS Collaboration, “Identification of heavy-flavour jets with the CMS detector in pp collisions at 13 TeV”, (2017). arXiv:1712.07158. Submitted to *JINST*.

- [49] D. Bertolini, P. Harris, M. Low, and N. Tran, “Pileup Per Particle Identification”, *JHEP* **10** (2014) 59, doi:10.1007/JHEP10(2014)059, arXiv:1407.6013.
- [50] B. A. Betchart, R. Demina, and A. Harel, “Analytic solutions for neutrino momenta in decay of top quarks”, *Nucl. Instrum. Meth. A* **736** (2014) 169, doi:10.1016/j.nima.2013.10.039, arXiv:1305.1878.
- [51] CMS Collaboration, “CMS Luminosity measurement for the 2016 data taking period”, CMS Physics Analysis Summary CMS-PAS-LUM-17-001, 2017.
- [52] CMS Collaboration, “CMS Luminosity measurement for the 2017 data taking period”, CMS Physics Analysis Summary CMS-PAS-LUM-17-004, 2017.
- [53] CMS Collaboration, “CMS Luminosity measurement for the 2018 data taking period”, CMS Physics Analysis Summary CMS-PAS-LUM-18-002, 2018.
- [54] ATLAS Collaboration, “Measurement of the inelastic proton-proton cross section at $\sqrt{s} = 13$ TeV with the ATLAS detector at the LHC”, *Phys. Rev. Lett.* **117** (2016) 182002, doi:10.1103/PhysRevLett.117.182002, arXiv:1606.02625.
- [55] CMS Collaboration, “Measurement of the top quark yukawa coupling from $t\bar{t}$ kinematic distributions in the lepton + jets final state in proton-proton collisions at $\sqrt{s} = 13$ tev”, *Phys. Rev. D* **100** (2019) 072007, doi:10.1103/PhysRevD.100.072007, arXiv:1907.01590.